NASA-CR-192784

FINAL REPORT

IMPROVED DETERMINATION OF VECTOR LITHOSPHERIC MAGNETIC ANOMALIES FROM MAGSAT DATA

(5/15/92-1/31/93)

GRANT
IN-46-CR
154194
p. 59

GRANT NO. NAG5-1972

Submitted to

National Aeronautics & Space Administration
Space Science Directorate
Goddard Space Flight Center
Greenbelt, MD 20771

January 1993

Dhananjay Ravat
Department of Geology
Southern Illinois University at Carbondale
Carbondale, IL 62901

IMPROVED DETERMINATION OF VECTOR LITHOSPHERIC MAGNETIC ANOMALIES FROM MAGSAT DATA

This final report describes scientific contributions made under NASA grant NAG5-1972 in developing new methods to isolate and map vector magnetic anomalies from measurements made by Magsat. In addition to the objective of the proposal, the isolation and mapping of equatorial vector lithospheric Magsat anomalies, we have tackled isolation of polar ionospheric fields during the award period. Significant progress has also been made in isolation of polar ΔZ component and scalar anomalies as well as integration and synthesis of various techniques of removing equatorial and polar ionospheric effects. This research has resulted in one invited published abstract and one manuscript is under preparation discussing the outcome of the research (to be submitted to a reviewed journal).

The significant contributions of this research are: 1) development of empirical/analytical techniques in modeling ionospheric fields in Magsat data and their removal from uncorrected anomalies to obtain better estimates of lithospheric anomalies. This task has been accomplished for equatorial ΔX, ΔZ, and ΔB component and polar ΔZ and ΔB component measurements; 2) integration of important processing techniques developed during the last decade with the newly developed technologies of ionospheric field modeling into an optimum processing scheme, and 3) implementation of the above processing scheme to map the most robust magnetic anomalies of the lithosphere (components as well as scalar).

The results of the research have been documented in an invited paper presented at the Fall 1992 American Geophysical Union meeting under:

Ravat, D., R. Langel, M. Purucker, T. Sabaka, J. Arkani-Hamed, D. Alsdorf, A new approach for isolation of lithospheric magnetic anomalies from Magsat, Invited paper, Eos Trans. AGU, 73, p.140, 1992.

These results are also being documented, to be published in a reviewed journal (under preparation), as:

Ravat, D., R. Langel, M. Purucker, J. Arkani-Hamed, and D. Alsdorf, Vector and scalar Magsat magnetic anomaly maps for geologic interpretation, in preparation.

The text of this manuscript describes the details of the procedures developed during the study and their results and, hence, is included as the remainder of the final report.

VECTOR AND SCALAR MAGSAT MAGNETIC ANOMALY MAPS FOR GEOLOGIC INTERPRETATION

INTRODUCTION

Satellite-derived magnetic anomalies are proving useful in mapping and understanding geologic evolution of large-scale tectonic features on the earth. These data have been used to map large-scale continental tectonic provinces (Frey, 1982; Arkani-Hamed and Strangway, 1985a; Ravat, 1989; Toft et al., 1992) and mineral resources (Taylor et al., 1992; Ravat et al., 1993), oceanic uplifts (Fullerton et al., 1989; Antoine and Moyes, 1992), magnetic quiet zones on the seafloor (LaBrecque and Raymond, 1985), and the nature and evolution of the Mesozoic break-up of Pangea (Frey et al., 1983; Galdeano, 1983; von Frese et al., 1986; Ravat et al., 1992).

Most researchers working with satellite magnetic data have used total intensity magnetic anomalies from the POGO and Magsat missions because of the relatively low error envelope of these data when compared with vector component data. Although Magsat measured three-orthogonal-component vector magnetic fields at an average altitude of approximately 400 km, the accuracy of the vector measurements depends largely on how well the directions of the magnetometer sensors are known (2-20 arc-sec). Thus, vector observations contain an inherent source of error (0.5-5 nT) beyond those in total intensity data (1-2 nT). The problem of accurate attitude determination is exacerbated by discontinuities or jumps in attitude solutions that result from changing the configuration of the attitude sensing instruments many times an orbit (Mayhew et al., 1985). Moreover, geologic anomalies are the residual of various large and small magnetic contributions to the measurements (e.g., Earth's main magnetic field, effects of magnetospheric and ionospheric currents, etc.). The precision of magnetic fields which represent geologic sources (referred interchangeably to as 'geologic', 'crustal', or 'lithospheric' magnetic anomalies in this paper) is thus limited by how well these other magnetic fields can be removed.

The problem faced is illustrated by the maps of Figures 1 and 2. As

described by Langel et al. (1982), the Magsat satellite acquired data only at twilight local times. Thus a natural division of that data into independent subsets is to treat dawn and dusk data separately (Arkani-Hamed et al., 1985; Yanagisawa and Kono, 1985). Figures 1 and 2 are residual maps of the total intensity anomalies of Magsat data at dawn and at dusk. The figures show ionospheric contamination in the form of anomaly bands that follow magnetic and geomagnetic latitudes in the low and high latitude regions, respectively. Data utilized in these maps has been selected from magnetically quiet times and low pass filtered (procedures to be described in detail in a later paragraph). A similar representation of the three vector component maps shows interesting patterns (not shown here). The ΔY map shows distinct positive residuals to the north and negative residuals to the south of the dip equator; similarly, the ΔZ map shows negative residuals to the north and positive residuals to the south of the dip equator; and the ΔX map shows a negative residual along the dip equator. Maeda et al. (1982, 1985) showed that this distinctive ΔY pattern is due to a meridional current associated with the equatorial electrojet. The ΔX and ΔZ patterns are consistent with an eastward flowing equatorial electrojet below the satellite. Data from dawn, especially ΔY, are relatively free from these effects, except as introduced by errors in deriving the residuals by removing a main field model (Langel et al., 1993).

Fortunately, many of the problems mentioned and illustrated in Figures 1 and 2 are not insurmountable. During the past decade, an arsenal of techniques has been developed and applied to both the scalar and vector data sets in attempts to isolate the geologic anomalies (Yanagisawa and Kono, 1984, 1985; Arkani-Hamed and Strangway, 1985a,b, 1986; Nakagawa and Yukutake, 1984, 1985; Nakagawa et al., 1985; Taylor and Frawley, 1987; von Frese et al., 1988; Cohen, 1989; Ravat, 1989; Cohen and Achache, 1990; Alsdorf, 1991; Purucker, 1991; Alsdorf et al., 1993; Langel et al., 1993; Ravat and Hinze, 1993). The authors of the present paper have separately been participants in developing portions of that arsenal of techniques. Recently, Langel (1992) called for a procedure in which several of these techniques are applied in a logical order. Partially in response to that suggestion, during the summer of 1992 the authors gathered at Goddard Space Flight Center in order to work as a team. The intent of the

present paper is to present the results of a concentrated team effort to collect together, refine, and, where necessary, extend existing techniques with the goal of deriving the best possible scalar and, especially, vector anomaly maps from Magsat data under the constraint of having to complete most of the work in a short period of time. The maps presented are not likely the ultimate vector anomaly maps: further improvements in isolation and resolution may be possible. Indeed, during this project we have identified areas of research and techniques (mainly for improved modeling of ionospheric and magnetospheric fields) that could possibly yield better resolved anomaly maps in the future. However, based on our combined experience, the maps presented here are a considerable improvement over those in the past and most probably describe fields geologic in origin which should be amenable to geologic interpretation.

In the following sections the methodology of how these techniques were applied to the data will be outlined, results from various stages of the process will be illustrated, and the final maps presented.

GENERAL DATA REDUCTION STRATEGIES

General Comments

If $\mathbf{B}(\mathbf{r},t)$ is the measured magnetic field at location $\mathbf{r}$ and time t then

$$\mathbf{B}(\mathbf{r},t) = \mathbf{M}(\mathbf{r},t) + \mathbf{A}(\mathbf{r}) + \mathbf{D}(\mathbf{r},t) + \varepsilon \qquad (1)$$

where $\mathbf{M}(\mathbf{r},t)$ is the field from Earth's core, the main field, $\mathbf{A}(\mathbf{r})$ is the field from Earth's crust, $\mathbf{D}(\mathbf{r},t)$ is the field from magnetospheric and ionospheric sources, including portions induced in Earth, and ε is the measurement error. In practice, analysis of both $\mathbf{A}(\mathbf{r})$ and $\mathbf{D}(\mathbf{r},t)$ begins by removing an estimate of $\mathbf{M}(\mathbf{r},t)$ from $\mathbf{B}(\mathbf{r},t)$. That estimate is from some model of the main field. The difference, or residual field is then

$$\Delta\mathbf{B}(\mathbf{r},t) = \mathbf{B}(\mathbf{r},t) - \mathbf{M}'(\mathbf{r},t) = \mathbf{A}(\mathbf{r}) + \mathbf{D}(\mathbf{r},t) + \eta \qquad (2)$$

where $\mathbf{M}'(\mathbf{r},t)$ is an estimate of $\mathbf{M}(\mathbf{r},t)$ and η is a combination of ε and model error. For crustal anomaly studies, $\mathbf{D}(\mathbf{r},t)$ and η constitute "noise".

The scalar residual field, or ΔB, is by definition

$$\Delta B(\mathbf{r},t) = |\mathbf{B}(\mathbf{r},t)| - |\mathbf{M}(\mathbf{r},t)|. \qquad (3)$$

Now, ignoring ε,

$$|\Delta \mathbf{B}| = [(\Delta \mathbf{B} + \mathbf{M}) \bullet (\Delta \mathbf{B} + \mathbf{M})]^{1/2} = [\Delta \mathbf{B} \bullet \Delta \mathbf{B} + 2\Delta \mathbf{B} \bullet \mathbf{M} + \mathbf{M} \bullet \mathbf{M}]^{1/2}. \qquad (4)$$

But $\Delta \mathbf{B} \bullet \Delta \mathbf{B}$ in (4) is much smaller than the other terms and can be neglected. Furthermore, the square root can be well approximated by the first two terms of its Taylor expansion. As a result

$$\Delta B = \Delta \mathbf{B} \bullet \mathbf{M} / |\mathbf{M}| \qquad (5)$$

is a good approximation (Note: $\Delta B \neq |\Delta \mathbf{B}|$).

Figure 3 is a flow-chart to summarize the data processing sequence. Important parameters used in application of a particular technique are given in Table 1. The following sections detail the process in the flow-chart and the reasons behind the choice of parameters. Choosing one technique over another designed for the same purpose is somewhat arbitrary and does not necessarily imply superiority of one technique over the other. Our choice is largely dictated by a judgement regarding the most suitable technique for the task in hand, but also involves complex considerations such as past experience with the technique, personal biases, and the democratic process.

During this project, known results of ionospheric and magnetospheric physics have been utilized as much as possible. In some instances, physical/empirical corrections have been directly applied (e.g., corrections for Equatorial Electrojet fields), in others they have been applied in an average sense (e.g., corrections applied for fields of ionospheric origin in polar regions). In other instances, the cause behind a particular variation

simply could not be unambiguously deduced (e.g., some low latitude seasonal-temporal effects at dawn local-time). However, even when a good measure of success was achieved in correcting for $\mathbf{D}(\mathbf{r},t)$, this study also has had to rely on statistical/signal processing methods to reduce discrepancies between maps.

Selection of Quiet Data

When deriving maps of crustal anomalies, $\mathbf{A}(\mathbf{r})$, it is sensible to begin with data from times of relatively magnetically quiet conditions, called "quiet data". How quiet depends on availability of sufficient data values with the chosen quiet criterion to make a map. Appropriate magnetic indices (see, e.g., Mayaud, 1980; Rangarajan, 1989) to choose quiet data are Kp (for equatorial and mid-latitude data) and AE (for polar data). Alternately or concurrently, one can use the variance of ΔB along a pass to judge the magnetic quietness of that pass. The premise in using the variance criterion is that $\mathbf{A}(\mathbf{r})$ is stationary and always present whereas external fields, $\mathbf{D}(\mathbf{r},t)$, are dynamic, with significant variation in amplitude from pass-to-pass, and always add energy (area under a residual profile curve) to magnetic observations. Profiles in the same location with less anomaly variance are least likely to be contaminated by $\mathbf{D}(\mathbf{r},t)$. The criteria used for the selection of quiet data are listed in Table 1. In choosing the variance cut-off for polar data, passes over a particular region are screened to ascertain that the cause of high variance was indeed $\mathbf{D}(\mathbf{r},t)$ and not $\mathbf{A}(\mathbf{r})$. One can determine that a pass has a large amount of $\mathbf{D}(\mathbf{r},t)$ contribution if, over the same track location, one finds another pass with significantly lower variance.

Main Field Removal

Accuracy in modeling $\mathbf{M}(\mathbf{r},t)$, including its secular variation is becoming increasingly important to the improvement of lithospheric component maps and to the represention of ionospheric contributions to

magnetic observations. Improper main field representation can introduce systematic variations in data, i.e. the η, that can be aliased as ionospheric current effects or lithospheric anomalies (Langel et al., 1993; Ravat and Hinze, 1993). Inclusion of even small amounts of the quietest equatorial dusk data in GSFC(12/83) field model (Langel and Estes, 1985a) led to a very small contamination (on the order of 2-5 nT) of that model in low latitudes in such a way as to introduce a systematic deviation in dawn vector Magsat data (Langel et al., 1993). For this reason, for the equatorial/mid-latitude segment of the data, a main field model was used which was derived by excluding dusk Magsat data (Dawn(6/83-6), Langel and Estes, 1985b). For polar data, however, the GSFC(12/83) field model (Langel and Estes, 1985a) was used.

Data were despiked for elimination of spurious values; over the poles, all selected passes were visually examined for spurious activity.

Removal of Vector Discontinuities

After the removal of $\mathbf{M}'(\mathbf{r},t)$, residual data were corrected for attitude solution jumps (Mayhew et al., 1985) which arise in processing of Magsat data. The attitude determination system on Magsat incorporated three sensors: two star trackers and a precision sun sensor. Finding the spacecraft attitude at any particular time involved a process of fitting the data from whichever sensors were contributing data at that time. If data were available from any two of the three sensors, an attitude solution was possible. However, the alignment between the three sensors was not perfectly known. As a result, whenever the available combination of sensors changed, a small discontinuity was introduced into the attitude solution. Many of the resulting field discontinuities are small, within 1 - 3 nT. A significant number, however, are larger and affect attempts to derive anomaly maps. We have used an empirical procedure developed by Purucker (1991) to adjust discontinuities in the magnetic component data. Illustration of the adjustments is shown in Figure 4.

Long-wavelength Filtering

Long-wavelength filtering is applied in this study to reduce the long-wavelength effects of ionospheric and magnetospheric currents. Ring-current is an equatorial sheet current that persists from two-to-three Earth radii out to Earth's magnetopause or magnetotail. Langel and Sweeney (1971) derived a potential function representation for the magnetic effect of this current that removes its major contribution in satellite magnetic observations. However, experience in applying this correction to satellite data has shown that the correction does not always center on the broad-scale minimum indicated by observations. As a result, the correction leaves behind residuals of both long- and short-wavelengths. Also, it is now apparent that many of the long-wavelength inconsistencies of equatorial Magsat data are related to equatorial electrojet and/or Sq fields, rather than magnetospheric fields. High-pass filtering, with wavelength-cut from 3000 to 5500 km according to the correlative nature of anomaly signal, has been implemented (Ridgway and Hinze, 1986; Baldwin and Frey, 1991) to remove long-wavelength residual artifacts from the ring-current and quiet day ionospheric currents, the Sq. As will be discussed, Langel et al. (1993) have successfully modeled many features of the magnetic field from the equatorial electrojet current system. This modeling required extension of the filter cut-off from about 4000 km to 12000 km for the equatorial/mid-latitude data. The filter selected was a "Kaiser" filter (Kaiser, 1974). The 12000 km wavelength cutoff does effectively remove magnetic effects of the ring-current and Sq.

In polar regions, however, modeling of $\mathbf{D}(\mathbf{r},t)$ is much more complicated and still in its infancy (for the purpose of deriving lithospheric magnetic anomalies). Hence, these data are filtered with a 4000 km wavelength high- pass Kaiser filter (Figure 3, Table 1). Similarly, scalar equatorial data have been filtered with the 4000 km cutoff because a different approach has been used to remove ionospheric effects in these data.

Identification of common signals: Correlation filtering

At several points in the procedure adopted for isolating A(r) a technique for identifying the common features in two data sets is required. One instance is to find the common signal from two satellite passes along identical, or nearly identical, tracks. The other is to find the common signal in two independent residual maps, either of some component or $\Delta B(r,t)$ or of $A(r)$.

Pass-by-pass correlation was used successfully by Alsdorf (1991) who pointed out that given the Fourier analyses of two signals of equal length, e.g.,

$$S_1 = \frac{1}{N} \sum_{k=0}^{N-1} A_k \, [\sin(kx) + \cos(kx)] \quad ,$$

$$S_2 = \frac{1}{N} \sum_{k=0}^{N-1} B_k \, [\sin(kx + t_k) + \cos(kx + t_k)] \quad , \qquad (6)$$

then the correlation coefficient between the k^{th} harmonics of the two analyses is given by

$$\rho_k = \cos(t_k) \qquad (7)$$

independently of the amplitudes of the Fourier components.

Spherical harmonic covariant correlation was developed by Arkani-Hamed and Strangway (1986) for analysis of scalar anomaly data but is applicable to analysis of any component of A(r), at a fixed altitude. That component is expressed in terms of spherical harmonics as follows

$$A_i(\theta,\phi) = \sum_{n=1}^{90} \sum_{m=0}^{n} [\, C^i_{nm} \cos(m\phi) + S^i_{nm} \sin(m\phi) \,] \; P^m_n (\cos\theta)$$

$$= \sum_{n=1}^{90} \sum_{m=0}^{n} [\, A^{i}_{nm} \cos(m\phi + \alpha^{i}_{nm}) \,]\; P^{m}_{n}(\cos\theta) \qquad (8)$$

where A_i is the i^{th} component of $\mathbf{A}(\mathbf{r})$ at colatitude θ and east longitude ϕ, $P^{m}_{n}(\cos\theta)$ are the Schmidt normalized associated Legendre functions of degree n and order m, and C_{nm} and S_{nm} are the spherical harmonic coefficients of the magnetic anomalies. $A_{nm} = [C_{nm}^2 + S_{nm}^2]^{1/2}$ is an amplitude factor and $\alpha_{nm} = \tan^{-1}(-S_{nm}/C_{nm})$, a phase factor. The corresponding power spectrum is defined by

$$P_n = \sum_{m=0}^{n} \frac{C_{nm}^2 + S_{nm}^2}{2n+1} \qquad (9)$$

The degree correlation between two such spherical harmonic analyses is defined by

$$\rho_n = \frac{\sum_{m=0}^{n} (C_{nm}\, C'_{nm} + S_{nm}\, S'_{nm})}{\{ [\sum_{m=0}^{n} (C_{nm}^2 + S_{nm}^2)] [\sum_{m=0}^{n} (C'^2_{nm} + S'^2_{nm})] \}^{1/2}} \qquad (10)$$

Given the analysis of dawn and dusk data according to equation (8), a correlation analysis can then be performed to isolate the "common" features of the dawn and dusk data, where "common" has an objective definition. To define "common", it is noted that, as in pass-by-pass correlation, a correlation coefficient for an individual degree and order between the two analyses can be defined as

$$\rho_{nm} = \cos(\alpha_{nm} - \alpha'_{nm}). \qquad (11)$$

The criteria chosen to identify "common" features between dawn and dusk is that $\rho_{nm} \geq 0.7$ and A_{nm} and A'_{nm} not differ by more than a factor of two. When this criteria is not met, the terms from that degree and order

are deleted from the analyses. This criteria was chosen after trying a suite of combinations. The choice is admitedly subjective. It is judged to preserve most of what are regarded as "common" features while succesfully rejecting most of the noise.

Advanced Processing

Advanced processing consists of various steps as dictated by physical processes controlling $\mathbf{D}(\mathbf{r},t)$ in a particular region and our ability to remove their magnetic effects. Here lies the heart of the present effort. Equatorial and polar regions pose specialized problems in modeling and reduction of satellite magnetic data and, therefore, these regions are treated separately. A generalized processing sequence (Figure 3) is as follows: an application and removal of physical/empirical correction for the appropriate ionospheric system (for equatorial electrojet, vector: Langel et al., 1993, scalar: Ravat and Hinze, 1993; for polar regions, this study), identification and retaining only the correlative components between nearby passes, i.e., pass-to-pass correlation, removal of cross-line differences between dawn and dusk intersecting profiles (Taylor and Frawley, 1987; Ravat, 1989), equivalent source inversion for the purpose of altitude-normalization (Dampney, 1969; Mayhew, 1979, von Frese et al., 1981; Langel et al., 1984, von Frese et al., 1988), spherical harmonic covariant correlation between dawn and dusk Magsat maps. A final equivalent source inversion is then used to compute common-altitude anomaly maps and effective volume susceptibility constrasts of the lithosphere.

Separation of fields from ionospheric and lithospheric sources. As noted, until recently the removal of $\mathbf{D}(\mathbf{r},t)$ has largely been treated as a signal processing problem. $\mathbf{A}(\mathbf{r})$ was considered to be the consistent part of the residual of the data processing sequence. Changing to a technique of modeling and removing $\mathbf{D}(\mathbf{r},t)$ was pioneered by Yanagisawa and Kono (1984, 1985) followed by Cohen and Achache (1990), whose methods have been modified and extended for part of the present analysis. The change to modeling and removing $\mathbf{D}(\mathbf{r},t)$ from data, even in part, requires effort to

ensure that the ionospheric model is not fitting a significant portion of $\mathbf{A}(\mathbf{r})$ as well. This issue is important, and difficult, because there is no clear or unambiguous separation between ionospheric and lithospheric magnetic anomalies in terms of their amplitude or wavelength characteristics.

In the present study, separation of $\mathbf{D}(\mathbf{r},t)$ from $\Delta\mathbf{B}(\mathbf{r},t)$ to isolate $\mathbf{A}(\mathbf{r})$ is carried out in a bootstrap, iterative manner. First an initial estimate of the crustal field was removed from $\Delta\mathbf{B}(\mathbf{r},t)$. Then, for each pass of retained data, an estimate of the form of $\mathbf{D}(\mathbf{r},t)$ was made along the track of the pass. The amplitude of that form was then determined by least squares fit of the form to the pass and the resulting, scaled $\mathbf{D}(\mathbf{r},t)$ subtracted from $\Delta\mathbf{B}(\mathbf{r},t)$ to give an estimate of $\mathbf{A}(\mathbf{r})$.

In the case of equatorial/mid-latitude data, the process utilized heavily the modeling of fields from the equatorial electrojet by Ravat and Hinze (1993) for scalar data and by Langel et al. (1993) for vector data.

For vector data, the underlying assumption of Langel et al. (1993) is that the sources and fields in question are organized with respect to the dip equator (see, e.g., Figures 1 and 2). First the data are filtered, pass-by-pass using a 12000 km cutoff high pass Kaiser filter. Langel et al. (1993) examined the extent of equatorial electrojet fields in dusk and dawn data and concluded that such effects were absent in dawn data except as dawn residuals were contaminated by the field model used to form the residuals. Accordingly, the initial estimate of $\mathbf{A}(\mathbf{r})$ was derived from Magsat dawn data.

The remaining procedures include fitting data from longitude swaths of 45° under the assumption that any remaining effects of $\mathbf{A}(\mathbf{r})$, or other contamination, will tend to be averaged out. This procedure was followed for both dawn and dusk data sets which were then transformed into dip latitude coordinates, where dip latitude is defined as $\delta = \tan^{-1}(0.5\tan I)$, where I is the geomagnetic inclination evaluated using the GSFC(12/83) field model (Langel and Estes, 1985a). One of two fitting procedures is then employed. In the first, the ΔB_θ and ΔB_r components are represented by the appropriate derivatives of a potential function of the form

$$V = a \sum_{n=1}^{N_t} \left(\frac{a}{r}\right) G_n P_n (\cos \theta_d) \qquad (12)$$

where $\theta_d = 90° - \delta$. Care was taken to avoid edge-effects at the poleward extremes of the data and N_t was chosen after a principal components analysis indicated which of the solution coefficients, the G_n, were significant. The G_n were dependent upon the daily sunspot number, R_d, according to $G_n = G'_n + G''_n * R_d$.

For ΔB_ϕ the data were fitted with the function

$$\Delta B_\phi = \frac{1}{(h-110)^\alpha} \sum_{n=0}^{N_t} G_n P_n (\cos \theta_d) \qquad (13)$$

where h is the altitude of the data point above the mean radius of Earth, and α is an empirically determined constant. Similar attention was given to edge-effects and N_t as for the analysis of equation (12).

A moving window approach in longitude was adopted with 128 windows, each of 45° width. This results in a shift of 2.8125° between windows. Seasonal variation was investigated by dividing the data into overlapping subsets of two month duration. Figure 5 shows the ΔB_θ and ΔB_r calculated from Equation (12) as based on data from March-April, 1980, in the longitude band 240°-300°. The error bars are the rms of the residual data to the field computed from Equation (12).

To "correct" $\Delta \mathbf{B}(\mathbf{r},t)$ for the effects of $\mathbf{D}(\mathbf{r},t)$ remaining after filtering, the appropriate two month period, sunspot number, and longitude bin from the data were identified and the $\mathbf{D}(\mathbf{r},t)$ from the analysis of Langel et al. (1993) computed along each pass. That $\mathbf{D}(\mathbf{r},t)$ was then scaled by keeping its form but scaling its amplitude by least squares fit to the measured $\Delta \mathbf{B}(\mathbf{r},t)$. The resulting scaled $\mathbf{D}(\mathbf{r},t)$ was subtracted from $\Delta \mathbf{B}(\mathbf{r},t)$.

A slightly different procedure (following Ravat and Hinze, 1993) was used in making ionospheric corrections for scalar equatorial anomaly data. The two differences in the procedures are (1) no initial estimate of crustal anomalies was removed from the scalar data when modeling ionospheric fields, and (2) the longitude swath in averaging scalar data was 90°. As for

vector data, guide functions of ionospheric field variations are constructed in the dip latitude - longitude space using moving window averages. As mentioned, the swath width was 90°; the step between windows was 1° longitude. As for vector data, the procedure was carried out for dawn and dusk data separately. These ionospheric guide functions, which are an approximation of $\mathbf{D}(\mathbf{r},t)$, were then least-squares scaled to data (i.e., ΔB or $\Delta B(\mathbf{r},t)$). To avoid over- scaling of $\mathbf{D}(\mathbf{r},t)$, in fitting $\mathbf{A}(\mathbf{r}) + \mathbf{D}(\mathbf{r},t)$ in the areas of strong lithospheric anomalies, Ravat and Hinze (1993) used an added constraint to the linear least-squares problem that the fit to ionospheric component must globally reduce cross-over differences between dawn and dusk total intensity observations. This method by-passed the effort required in first removing an estimate of crustal anomalies from data.

The above described process was carried out for all components of $\Delta B(\mathbf{r},t)$ and for $\Delta B(\mathbf{r},t)$, the scalar residual.

At high latitudes, i.e., the auroral belt in particular, $\mathbf{D}(\mathbf{r},t)$ is much more complex than at low and mid latitudes. In particular, ΔX and ΔY show extremely large and variable behavior in the auroral belts due to the presence of field aligned currents. Although an attempt was made, the techniques available to us did not prove adequate to isolate what could be regarded as a reliable estimate of the anomaly field in these components. Accordingly, the high latitude analyses to be described apply only to ΔB and to ΔZ. Figure 6 illustrates problems faced in the high latitude regions, where ΔB_r (i.e., $-\Delta Z$) component shows distinct anomaly patterns systematic in geomagnetic latitudes. It is also apparent from these maps that the uncorrected anomalies are also significantly different for the two data subsets for each of the polar region.

Also, in the case of high latitude data, because of its high dependence on solar activity and consequent variability, a robust first estimate of lithospheric magnetic anomalies could only be obtained through quantitative comparisons of data sets having different observational characteristics (e.g., different local-times, altitude ranges, etc.). Hence, a spherical harmonic covariance correlation of signal from the dawn and dusk quiet subsets was used as the initial estimate of crustal anomalies.

A major difference between the equatorial/mid latitude region analysis and the analysis for the polar regions lies in the systematics of the auroral ionospheric fields (i.e., their representation in terms of an optimum

coordinate system). In the case of the equatorial/mid-latitude twilight Magsat data, it was possible to organize ionospheric variations with respect to magnetic (dip) latitudes. However, in the polar ionosphere, geomagnetic (dipole) latitude, or a refinement thereof, controls the organization of electrical currents and consequently their magnetic effects. Another important difference, for Magsat data, is that as the satellite orbit traversed the polar regions, because it was not in a strictly polar orbit it sampled a range of local-times rather than just dawn and dusk. In geomagnetic coordinates this difference is even more pronounced because of the 11.2° tilt of the geomagnetic coordinate system with respect to Earth's rotation axis. Data organization for study and representation of the resulting magnetic fields must take into account that ionospheric current morphology in auroral and polar regions strongly depends on the magnetic local time (MLT). Thus, after subtracting the initial estimate of $\mathbf{A}(\mathbf{r})$ from $\Delta\mathbf{B}(\mathbf{r},t)$, the data averages were compiled in roughly 2° by 2° equal-area bins in the dipole latitude - MLT coordinate system. The results for ΔB for the northern hemisphere dawn and dusk data are shown in Figure 7. The premise is that such averages are an estimate of the average ionospheric field, i.e. constitute an $\mathbf{D}'(\mathbf{r})$, and can be used to at least partially correct $\Delta\mathbf{B}(\mathbf{r},t)$ for the effects of $\mathbf{D}(\mathbf{r},t)$.

The correction of $\Delta\mathbf{B}(\mathbf{r},t)$ by $\mathbf{D}'(\mathbf{r})$ is accomplished similarly to the procedure for equatorial and low latitudes. Along each pass the values of $\mathbf{D}'(\mathbf{r})$ are collected and a common scaling factor, say s, determined for that pass such that the scaled $\mathbf{D}'(\mathbf{r})$ best fits $\Delta\mathbf{B}(\mathbf{r},t)$ in a least squares sense. Then the estimate of the crustal field is $\mathbf{A}'(\mathbf{r}) = \Delta\mathbf{B}(\mathbf{r},t) - \mathbf{D}'(\mathbf{r})$. As previously noted, this procedure was carried out for ΔB and for ΔZ. Figures 8 and 9 show ionospheric field corrected dawn and dusk ΔB anomaly maps, respectively (to be compared with Figures 1 and 2).

Processing to improve signal-to-noise ratio, altitude normalization, and gridding. Continuing the description of the flowchart in Figure 3, the stage has been reached where as much has been done as is possible to remove the effects of $\mathbf{D}(\mathbf{r},t)$ from $\Delta\mathbf{B}(\mathbf{r},t)$. However, at this stage, there still are apparent inconsistencies between nearby passes and between dawn and dusk data sets. The premise for further data processing is that lithospheric or crustal anomalies should be consistent (not necessarily the same)

between nearby passes and should be identical (in practice, similar) regardless of measurement time. The purpose of this phase of the processing is to extract such common components from data (signal) and suppress variable components (noise). It is important to note that if the ionospheric components have similar wavenumber and amplitude characteristics between two data sets being compared, the processing will not be able to distinguish their nature: at this stage, it is assumed that this distinction was made by the earlier corrections.

We have compiled maps and statistical parameters showing improvements resulting from our processing at various processing steps and each of the components (e.g, dawn-dusk difference maps, maps of correlation between dawn and dusk 220 km x 220 km equal-area averages, and histograms of the above average anomaly differences). However, it is impractical to show all of these parameters at each of the processing steps and for each component. And hence, only the improvements due to ionospheric field corrections are shown in the map form for ΔB 220 km x 220 km equal-area averages; the parameter chosen here is the dawn-dusk difference (Figure 10a and b). The remaining processing improvements are shown, once again for ΔB, as histograms of the above dawn-dusk average differences (Figure 11).

To improve the consistency of data (signal) between two nearby passes, the pass-by-pass correlation technique (Alsdorf, 1991), described earlier, was used. As noted, the commonalities between two equal- length profiles can be quantitatively compared, i.e., a correlation coefficient derived, for each wavenumber. Admittance criteria for a particular degree of correlation, however, are qualitative. For example, two profiles with identical spatial locations should be required to correlate with high degree of correlation; as the distance between the profiles increases, the assumption of two dimensionality of anomalies perpendicular to the direction of the profiles is lost and the wavenumber with lower correlation coefficients cannot be automatically rejected as noise. After experimentation with a range of correlation coefficient cut-off criteria and their effect on all the different segments of the anomaly maps, wavenumbers with correlation coefficients of 0.3 and above were retained for all dawn/dusk and equatorial/polar data segments. A considerable improvement has been realised due to the implementation of the pass-by-

pass correlation technique for each of the data subsets (Figures 12 and 13; to be compared.with Figures 8 and 9)

After completing adjustments to the data from intercomparing adjacent passes, an analysis was conducted of the crossover differences between dawn and dusk passes. The purpose of adjusting cross-line differences (Taylor and Frawley, 1987; Ravat, 1989) was to adjust simultaneously the levelling inaccuracies between the profiles within the individual data sets and between the dawn and the dusk subsets. In this study, the cross-line adjustments were implemented only on equatorial/mid-latitude data.

At this point the, multiply corrected, data are spaced unevenly in position, including altitude. This introduces artificial noise when the data are averaged and when comparing dawn and dusk data which are at differing altitudes. Also, processing of the three components at each local time has to this point proceeded independently. The next step in the process is to derive equivalent point dipole representations which can be used to reduce the data to common elevation and to facilitate further intercomparison of data from the two local times.

Derivation of this representation was inspired by Dampney's (1969) method for synthesizing Bouguer gravity measurements on an irregular three dimensional grid. The synthesis consisted of a mathematical representation of the data in terms of discrete point masses at some, arbitrary, fixed depth below the Earth's surface. Mayhew (1979) adapted this method to the synthesis of magnetic anomaly data acquired by the POGO satellites. In this method the satellite magnetic anomaly data are represented by an array of dipoles at the Earth's surface. The dipoles are assumed to be aligned along the direction of the Earth's main field, as determined by a spherical harmonic model, and their magnitudes are determined so as to best reproduce the anomaly data in a least-squares sense. Following Dampney, this is called an equivalent source model. Working independently, von Frese et al. (1981) proposed the same method of analysis, only applied to gravity as well as magnetic anomaly data.

Such inversions were performed, separately for dawn and dusk data, for the combined, corrected, ΔZ and ΔX data, except at high latitudes where only ΔZ were included. Inversion was also performed for the ΔB data. The ΔY component was not used for two reasons. First, because even after

application of the corrections described above, ΔY for dusk was judged to still be contaminated to an unacceptable amount. Second, because the very clean dawn ΔY, at low and mid latitudes, can be used as an independent test of the validity of the equivalent source solution. Examples of ΔB dawn and dusk anomalies at 400 km elevation after the inversion are shown in Figures 14 and 15, respectively.

The inversion also allows recomputation of anomalies at common altitude and at specified grid intervals as required for the application of Spherical harmonic covariant correlation previously described. Spherical harmonic covariant correlation provides a powerful tool for further comparison and consistency improvement between the dawn and the dusk data sets. As mentioned earlier, the technique is used for retaining commonalities in maps rather than profiles and suppressing the contribution made by undesirable harmonics (as apparent from their small correlation coefficients and differences in amplitudes). Figure 16 shows correlation coefficients between the dawn and the dusk anomaly maps for each harmonic degree for each of the anomaly components before and after the selection of criteria for common characteristics (correlation coefficients $\geq$ 0.7 and amplitude factors A_{nm}'s within factor of two). As described earlier, coefficients that do not meet these criteria are deleted from the analysis. It is apparent from the spectra in Figure 16 that before the above selection the correlation coefficients are much lower than 1.0 (solid lines), indicating that there is residual external field contamination in the two maps. After the selection, however, the two signals (maps) are seen to correlate to a high level (long-short dashed line in Figure 16). Figures 17 and 18 show the power at each degree harmonic for dawn and dusk maps, respectively, and for each of the components before and after the process. It can be observed from these figures that most of the original power is retained by the analysis, reduction of power being limited to non-correlative parts between the two corresponding data sets.

After the spherical harmonic correlation analysis, all processed data sets were subject to simultaneous inversions (vector and scalar separately) from which final vector and scalar anomalies have been computed at 400 km (Figure 19).

SUMMARY

Vector and scalar magnetic anomaly maps have been prepared from Magsat data using a systematic approach that integrates a variety of useful processing schemes developed during the last decade. The approach initially focuses on modeling and removal of ionospheric magnetic fields in both equatorial and polar regions and subsequently relies on signal processing techniques to minimize remaining discrepancies between data measured at different local-times, the premise being the lithospheric anomalies should be consistent regardless of the measurement time. This technique has resulted in identifying the most robust Magsat magnetic anomalies that are most likely lithospheric in origin (Figure 19). As a corollary, the anomalies that do not appear on these maps but appear in other published maps that have been prepared without taking into account the ionospheric contamination are less robust and therefore such anomalies should be carefully scrutinized for ionospheric contamination and repeatability before they are interpreted.

In addition to the mapping of the most robust satellite magnetic anomalies, new techniques have been devised to model polar ionospheric fields in ΔZ and ΔB components and to map polar magnetic anomalies from satellites that were hitherto untenable because of the large ionospheric contamination in the polar regions. Moreover, for the first time, analytical vector equatorial ionospheric corrections were used to map equatorial lithospheric magnetic anomalies.

Thus, significant progress has been made during the award period in analyzing and modeling ionospheric fields in Magsat data and devising techniques to map most repetitive Magsat magnetic anomalies of the lithosphere. The techniques developed during this project are also applicable for the analysis of future low altitude satellite magnetic data sets and would prove invaluable in their initial analysis.

REFERENCES

Alsdorf, D.E., 1991, Statistical processing of Magsat data for magnetic anomalies of the lithosphere, M.S. Thesis, The Ohio State University, Columbus, Ohio, 173p.

Alsdorf, D.E., R.R.B. von Frese, J. Arkani-Hamed, and H.C. Noltimier, 1993, Separation of lithospheric, external and core components of the geomagnetic field at satellite altitudes, J.Geophys.Res., submitted.

Antoine, L.A.G. and A.B. Moyes, 1992, The Agulhas Magsat anomaly: implications for continental break-up of Gondwana, Tectonophysics, 212, 33-44.

Arkani-Hamed, J. and D.W. Strangway, 1985a, Intermediate-scale magnetic anomalies of the earth, Geophysics, 50, 2817-2830.

Arkani-Hamed, J. and D.W. Strangway, 1985b, Lateral variations of apparent susceptibility of lithosphere deduced from Magsat data, J. Geophys. Res., 90, 2655-2664.

Arkani-Hamed, J. and D.W. Strangway, 1986, Band-limited global scalar magnetic anomaly map of the Earth derived from Magsat data, J. Geophys. Res., 91, 8193-8203.

Arkani-Hamed, J., W.E.S Urquhart, and D.W. Strangway, 1985, Scalar magnetic anomalies of Canada and northern United States derived from Magsat data, J. Geophys. Res., 90, 2599-2608.

Baldwin, R. and H. Frey, 1991, Magsat crustal anomalies for Africa: dawn and dusk data differences and a combined data set, Phys. Earth Planet. Int., 67, 237-250.

Cohen, Y., 1989, Traitements et interpretations de donnees spatiales en geomagnetisme: etude des variations laterales d'aimantation de la lithosphere terrestre, Ph.D. Thesis University of Paris VII and Institute de physique du globe de Paris.

Cohen, Y., and J. Achache, 1990, New global vector magnetic anomaly maps derived from Magsat data, J.Geophys.Res., 95, 10783-10800.

Dampney, C.N.G., 1969, The equivalent source technique, Geophysics, 34, 39-53.

Frey, H., 1982, Magsat scalar anomaly distribution: the global perspective, Geophys. Res. Lett., 9, 277-280.

Frey, H., R. Langel, G. Mead, and K. Brown, 1983, POGO and Pangaea, Tectonophysics, 95, 181- 189.

Fullerton, L.G., H.V. Frey, J.H. Roark, and H.H. Thomas, 1989, Evidence for a remanent contribution in Magsat data from the Cretaceous quiet zone in the South Atlantic, Geophys.Res.Lett., 16, 1085-1088.

Galdeano, A., 1983, Acquisition of long wavelength magnetic anomalies predates continental drift, Phys.Earth Planet. Int., 32, 289-292.

Kaiser, J.F., 1974, Nonrecursive digital filter design using the Io-sinh window function, Proc. 1974 IEEE Int. Symp. Circuits and Systems, 20-23.

LaBrecque, J.L., and C.A. Raymond, 1985, Seafloor spreading anomalies in the Magsat field of the North Atlantic, J.Geophys.Res., 90, 2565-2575.

Langel, R.A., 1992, The use of low altitude satellite data bases for modeling of core and crustal fields and the separation of external and internal fields, Surveys in Geophysics, in press.

Langel, R.A., and R.H. Estes, 1985a, The near-earth magnetic field at 1980 determined from Magsat data, J.Geophys.Res., 90, 2495-2510.

Langel, R.A., and R.H. Estes, 1985b, Large-scale, near-earth magnetic fields from external sources and the corresponding induced internal field, J.Geophys.Res., 90, 2487-2494.

Langel, R.A., and R.A. Sweeney, 1971, Asymmetric ring current at twilight local time, J.Geophys.Res., 76, 4420-4427.

Langel, R.A., M. Purucker, and M. Rajaram, 1993, The equatorial electrojet and associated currents as seen in Magsat data, J. Atm. Terr. Phys., in press.

Langel, R.A., E.V. Slud, and P.J. Smith, 1984, Reduction of satellite magnetic anomaly map from Magsat, J.Geophysics, 54,207-212.

Langel, R.A., G. Ousley, J. Berbert, J. Murphy, and M. Settle, 1982, The Magsat mission, Geophys. Res. Lett., 9, 243-245.

Maeda, H., T. Kamei, T. Iyemori, and T. Araki, 1985, Geomagnetic perturbations at low latitudes observed by Magsat, Jour. Geophys. Res., 90, 2481-2486.

Maeda, H., T. Iyemori, T. Araki, and T. Kamei, 1982, New evidence of a meridional current system in the equatorial ionosphere, Geophys. Res. Lett., 9, 341-344.

Mayaud, P.N., 1980, Derivation meaning and use of geomagnetic indices, Geophysical Monograph 22, AGU, Washington D.C..

Mayhew, M.A., 1979, Inversion of satellite magnetic anomaly data, J.Geophysics, 45, 119-128.

Mayhew, M.A., B.D. Johnson, and P.J. Wasilewski, 1985, A review of problems and progress in studies of satellite magnetic anomalies, J.Geophys.Res., 90, 2511-2522.

Nakagawa, I., and T. Yukutake, 1985, Rectangular harmonic analysis of geomagnetic anomalies derived from Magsat data over the area of the Japanese islands, J. Geomag. Geoelectr., 37, 957-977.

Nakagawa, I., and T. Yukutake, 1984, Spatial properties of the geomagnetic field over the area of the Japanese Islands deduced from Magsat data, J. Geomag. Geoelectr., 36, 443-453.

Nakagawa, I., T. Yukutake, and N. Fukushima, 1985, Extraction of magnetic anomalies of crustal origin from Magsat data over the area of the Japanese islands, Jour. Geophys. Res., 90, 2609-2616.

Purucker, M.E., 1991, The correction of attitude solution jumps in the Magsat data set, Unpublished manuscript, 20p.

Rangarajan, G.K., 1989, Indices of geomagnetic activity, in:J.A. Jacobs (ed.), Geomagnetism, Vol. 3, Chap. 5, Academic Press, London.

Ravat, D., 1989, Magsat investigations of the greater African region, Ph.D. dissertation, Purdue University, West Lafayette, Indiana, 234p.

Ravat, D., and W.J. Hinze, 1993, Considerations of variations in ionospheric fields effects in mapping equatorial lithospheric Magsat magnetic anomalies, Geophys.J.Int., in press.

Ravat, D., W.J. Hinze, and P.T. Taylor, 1993, European tectonic features observed by Magsat, Tectonophysics, in press.

Ravat, D., W.J. Hinze, and R.R.B. von Frese, 1992, Analysis of Magsat magnetic contrasts across Africa and South America, Tectonophysics, 212, 59-76.

Ridgway, J.R., and W.J. Hinze, 1986, Magsat scalar anomaly map of South America, Geophysics, 51, 1472-1479.

Taylor, P.T., and J.J. Frawley, 1987, Magsat anomaly data over the Kursk magnetic region, USSR, Phys.Earth Planet. Int., 45, 255-265.

Taylor, P.T., W.J. Hinze, and D. Ravat, 1992, The search for crustal resources: Magsat and beyond, Adv. Space Res., 12, (7)5-(7)15.

Toft, P.B., P.T. Taylor, J. Arkani-Hamed, and S.E. Haggerty, 1992, Interpretation of satellite magnetic anomalies over the West African Craton, Tectonophysics, 212, 21-32.

von Frese, R.R.B., D.N. Ravat, W.J. Hinze, and C.A. McGue, 1988, Improved inversion of geopotential field anomalies for lithospheric investigations, Geophysics, 53, 375-385.

von Frese, R.R.B., W.J. Hinze, R. Oliver, and C.R. Bentley, 1986, Regional magnetic anomaly constraints on continental breakup, Geology, 14, 68-71.

von Frese, R.R.B., W.J. Hinze, and L.W. Braile, 1981, Spherical earth gravity and magnetic anomaly analysis by equivalent point source inversion, Earth Planet. Sci. Lett., 53, 69-83.

Yanagisawa, M. and M. Kono, 1985, Mean ionospheric field correction for Magsat data, J. Geophys. Res., 90, 2527-2536.

Yanagisawa, M., and M. Kono, 1984, Magnetic anomaly maps obtained by means of the mean ionospheric field correction, J.Geomagn.Geoelectr., 36, 417-442.

Table 1. Processing parameters (see processing flowchart, Fig. 3):

Process	Equatorial vector	Equatorial scalar	Polar
Quiet selection	Kp ≤ 1+	Kp ≤ 2+	AE ≤ 50 nT ΔBvar ≤ 80 nT^2
Main Field	Dawn 6/83-6	Dawn 6/83-6	GSFC 12/83
High-pass (λ)	12000 km	4000 km	4000 km
No. of Iterations of ionospheric field removal	1	N/A	1
Pass-to-pass	cc ≥ 0.3	N/A	cc ≥ 0.3
Cross-line adjustments	zero order	zero order	none
Covariant spher. harmonics	cc ≥ 0.3 Ampl. fact. = 2	cc ≥ 0.3 Ampl. fact. = 2	cc ≥ 0.3 Ampl. fact. = 2

FIGURES

Figure 1. Total intensity anomaly (residual) map from Magsat dawn data prior to ionospheric corrections. Units are nT. CI = 2 nT. Van Der Grinten projection.

Figure 2. Total intensity anomaly (residual) map from Magsat dusk data prior to ionospheric corrections. Units are nT. CI = 2 nT. Van Der Grinten projection.

Figure 3. Flow chart of Magsat data processing.

Figure 4. Illustration of correction of attitude jump in Magsat data. x x x indicates original ΔZ data; solid line indicates corrected data.

Figure 5. Computed values of ΔZ (top) and ΔX (bottom) from Equation (12) for the longitude range 240-300° during March-April, 1980. The ordinate is dip latitude; the abcissa is in nT. The error bars reflect the 1 standard deviation scatter of the data used in the fit from the values computed from Equation (12).

Figure 6. ΔB_r component anomalies over polar regions showing the bands of anomalies systematically along geomagnetic latitudes. (a) north polar, dawn; (b) north polar, dusk; (c) south polar, dawn; (d) south polar, dusk.

Figure 7. Averages of ionospheric field, $\mathbf{D'(r,t) = \Delta B(r,t) - A'(r)}$, for ΔB component in MLT-geomagnetic (dipole) latitude coordinates. $\mathbf{A'(r)}$ is the initial estimate of $\mathbf{A(r)}$. Units are nT. CI = 2 nT. (a) north polar, dawn; (b) north polar, dusk; (c) south polar, dawn; (d) south polar, dusk.

Figure 8. Ionospheric field corrected anomaly map of ΔB from Magsat dawn data. Units are nT. CI = 2 nT. Van Der Grinten projection.

Figure 9. Ionospheric field corrected anomaly map of ΔB from Magsat dusk data. Units are nT. CI = 2 nT. Van Der Grinten projection.

Figure 10. Difference map of dawn-dusk 220 km x 220 km equal-area averages of ΔB. CI = 2 nT. Van Der Grinten projection. (a) before ionospheric corrections; (b) after ionospheric corrections.

Figure 11. Histograms of ΔB dawn-dusk differences before and after ionospheric corrections. (a) north polar; (b) equatorial; (c) south polar.

Figure 12. Dawn ΔB anomaly map after pass-by-pass correlation. CI = 2 nT. Van Der Grinten projection.

Figure 13. Dusk ΔB anomaly map after pass-by-pass correlation. CI = 2 nT. Van Der Grinten projection.

Figure 14. Dawn ΔB anomaly map at 400 km after equivalent source inversion. CI = 2 nT. Van Der Grinten projection.

Figure 15. Dusk ΔB anomaly map at 400 km after equivalent source inversion. CI = 2 nT. Van Der Grinten projection.

Figure 16. Degree correlation between final dawn and dusk maps. (a) ΔZ; (b) ΔX; (c) ΔY; (d) ΔB.

Figure 17. Power spectra of dawn anomaly maps. (a) ΔZ; (b) ΔX; (c) ΔY; (d) ΔB.

Figure 18. Power spectra of dusk anomaly maps. (a) ΔZ; (b) ΔX; (c) ΔY; (d) ΔB.

Figure 19. Combined corrected anomaly map from Magsat data. Units are nT. CI = 2 nT. (a) ΔZ; (b) ΔX; (c) ΔY; (d) ΔB.

DAWN AVERAGES

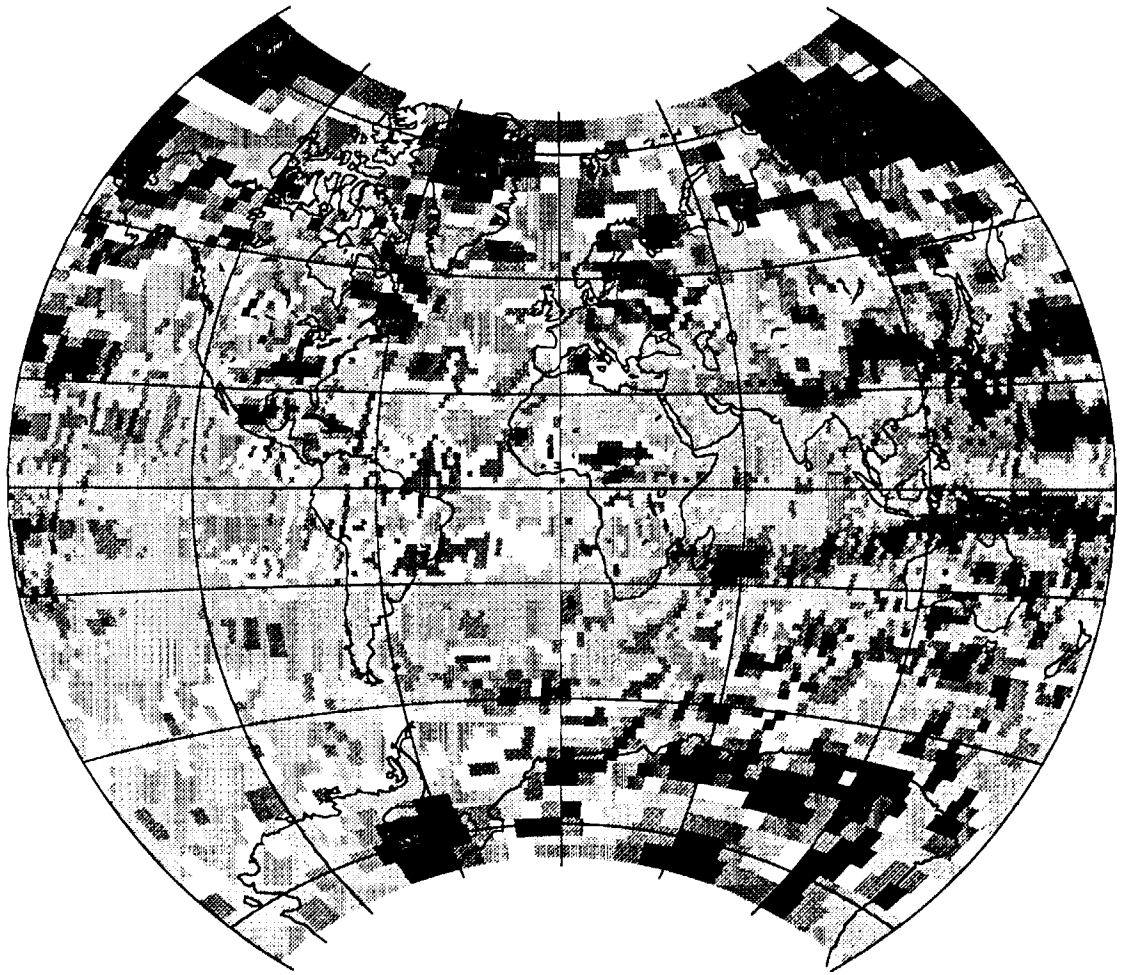

Prior to ionospheric field removal

tikustat.f 11-19-92 cbbins.bincomb

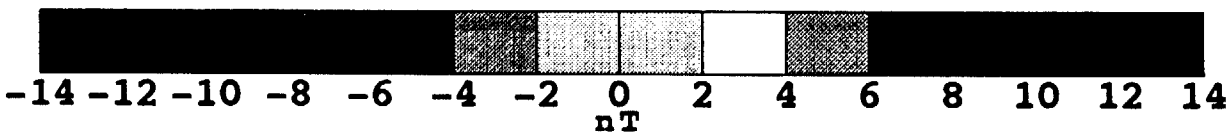

FIG. 1

DUSK AVERAGES

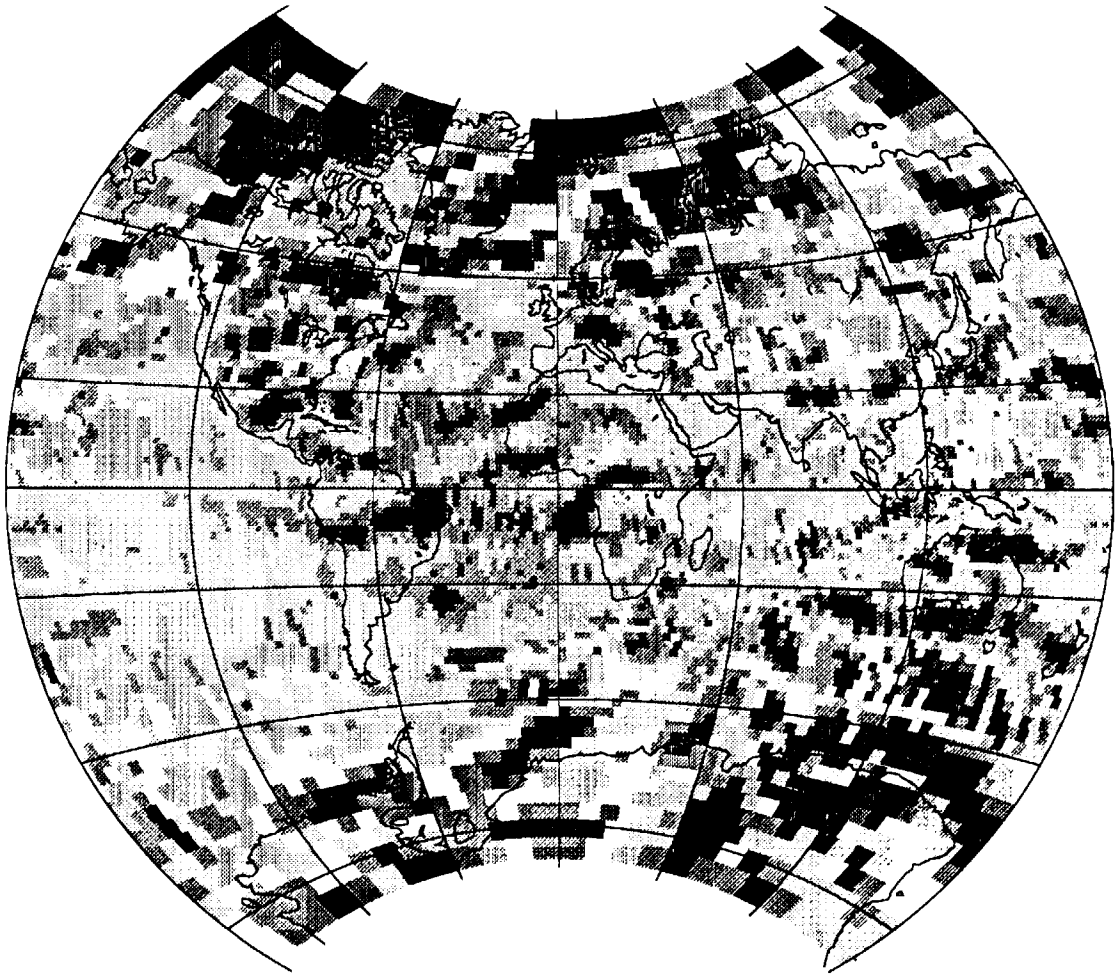

Prior to ionospheric field removal

tikustat.f 11-19-92 cbbins.bincomb

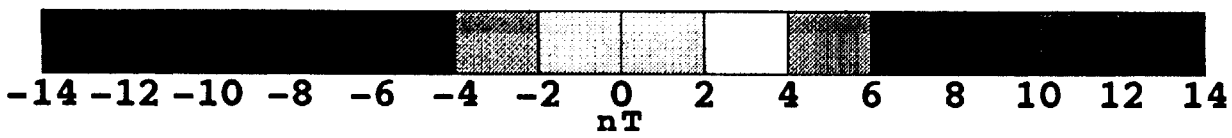

FIG. 2

FLOW-CHART OF MAGSAT DATA PROCESSING

(* : keyed to parameters in Table 1)

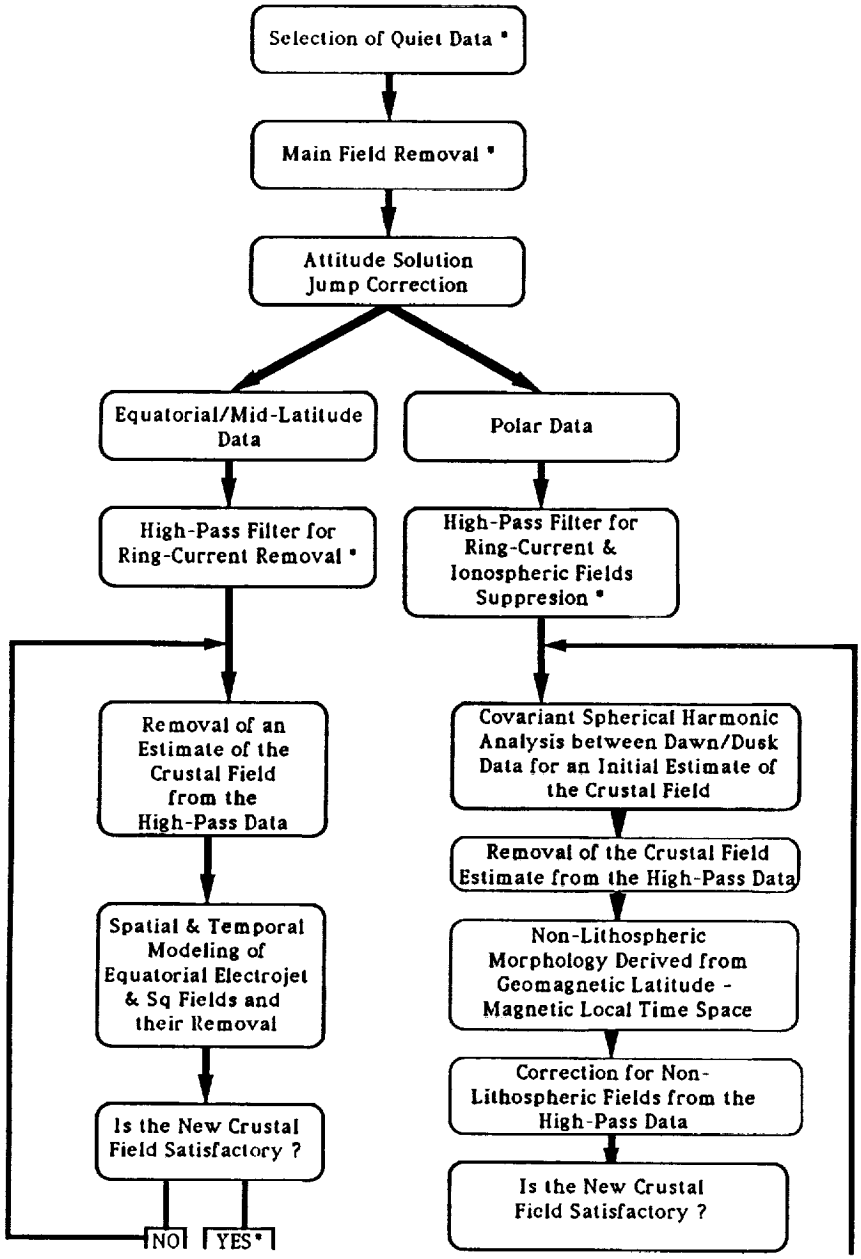

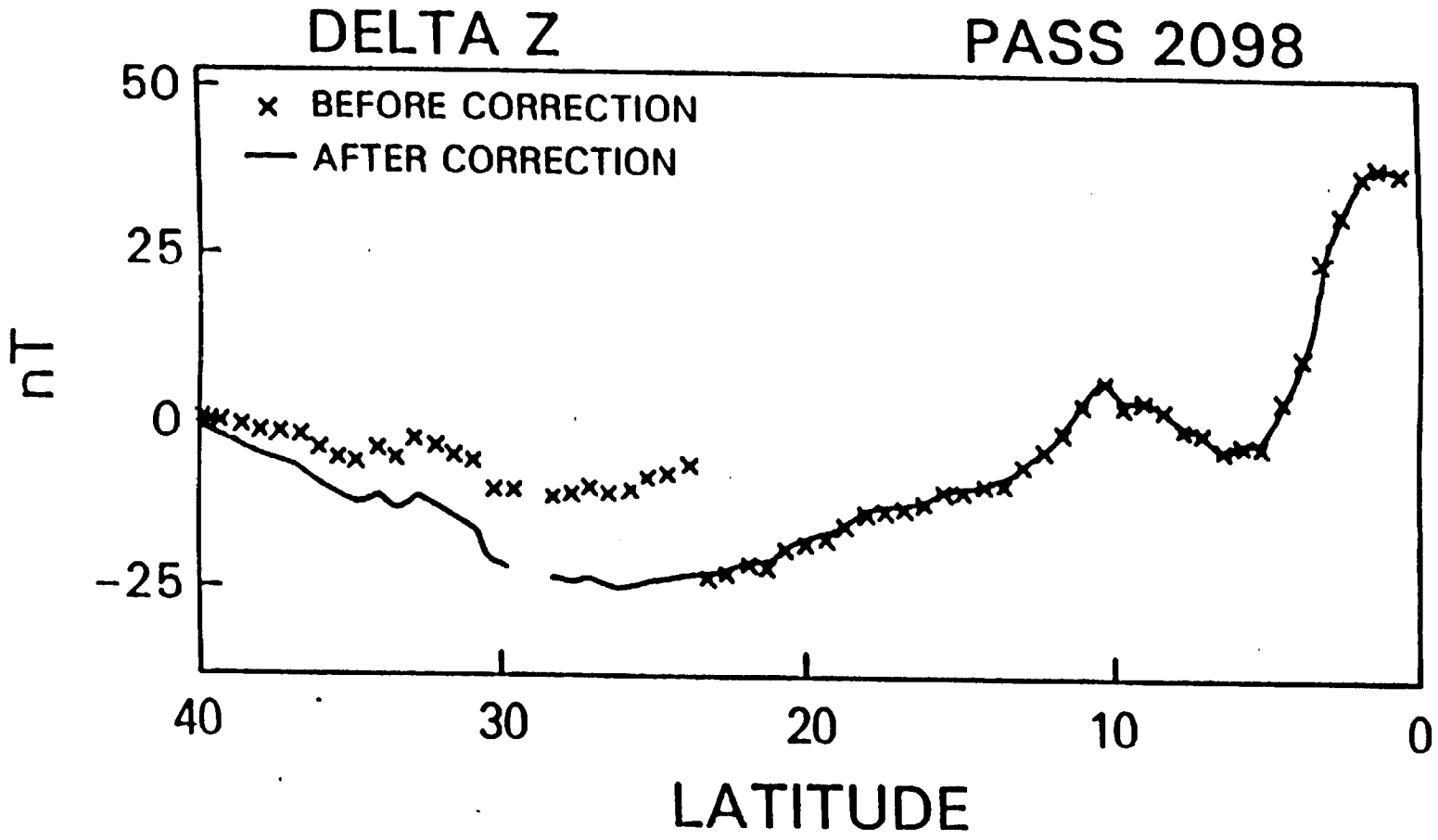
DELTA Z
PASS 2098
× BEFORE CORRECTION
— AFTER CORRECTION
50
25
0
-25
nT
40
30
20
10
0
LATITUDE

FIG. 4

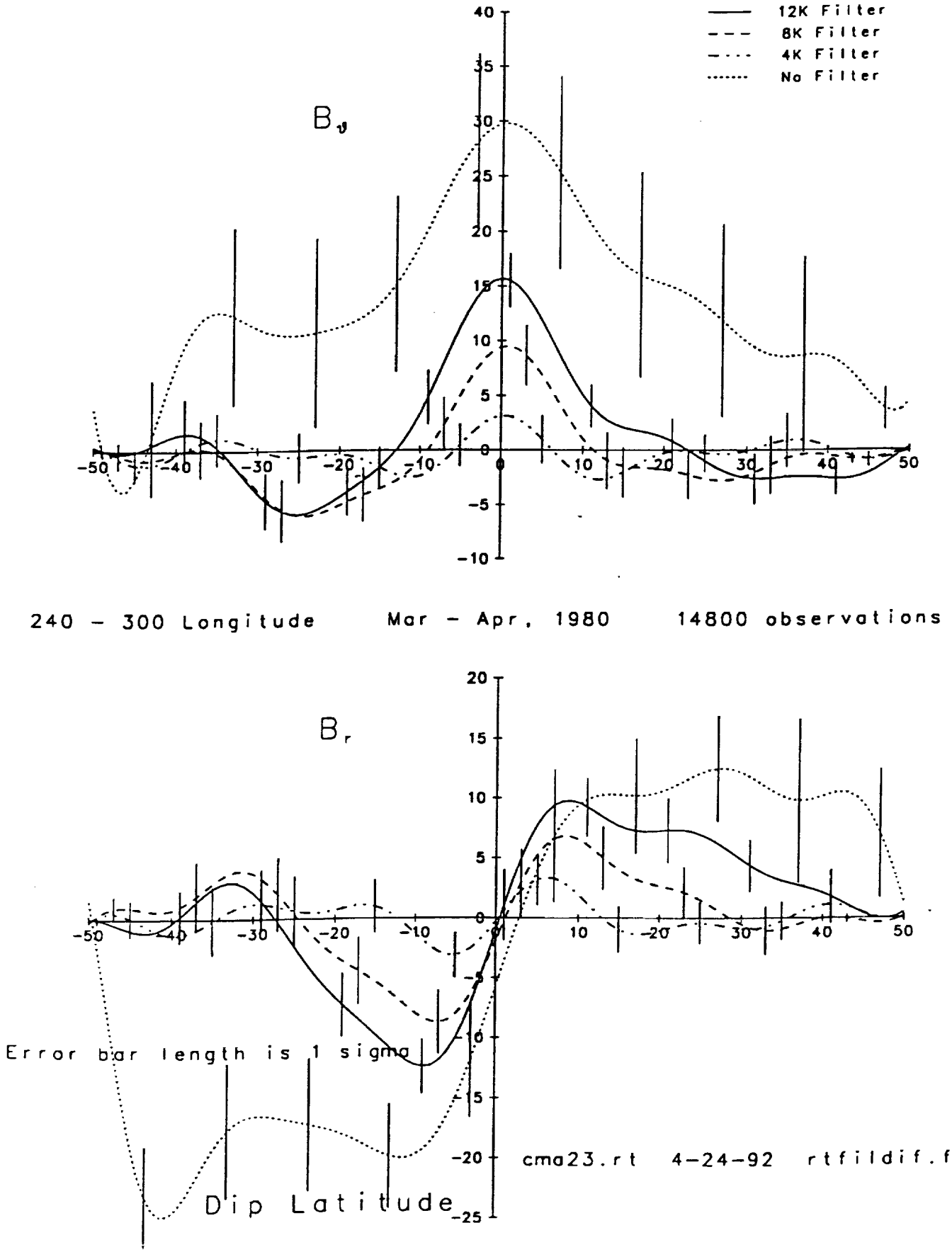
12K Filter
8K Filter
4K Filter
No Filter
B_ϑ
240 – 300 Longitude
Mar – Apr, 1980
14800 observations
B_r
Error bar length is 1 sigma
cma23.rt 4-24-92 rtfildif.f
Dip Latitude

FIG. 5

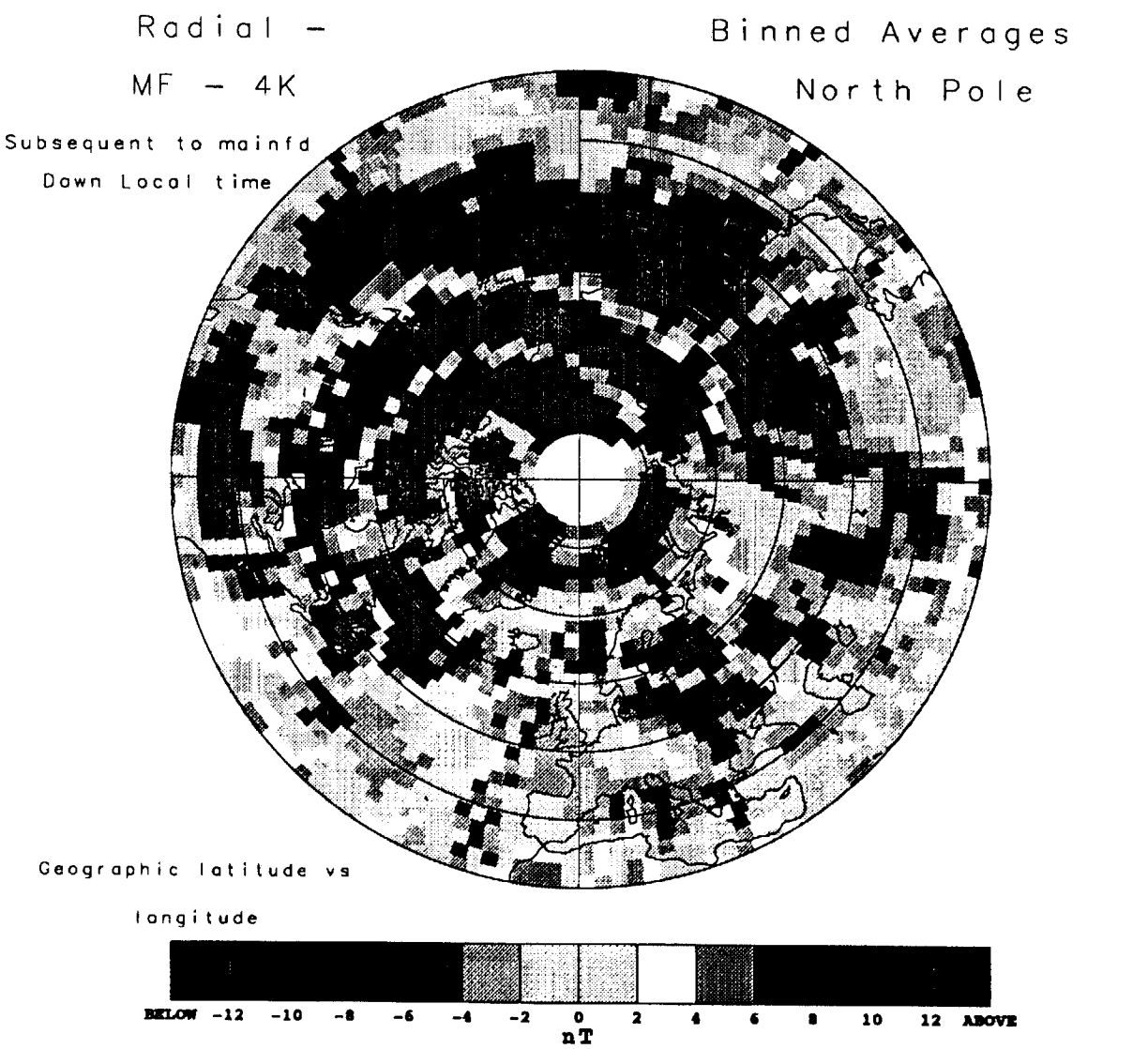
Radial –
MF – 4K
Subsequent to mainfd
Down Local time
Binned Averages
North Pole
Geographic latitude vs
longitude
BELOW -12 -10 -8 -6 -4 -2 0 2 4 6 8 10 12 ABOVE
nT
npolebin.f 11-14-92

FIG. 6a

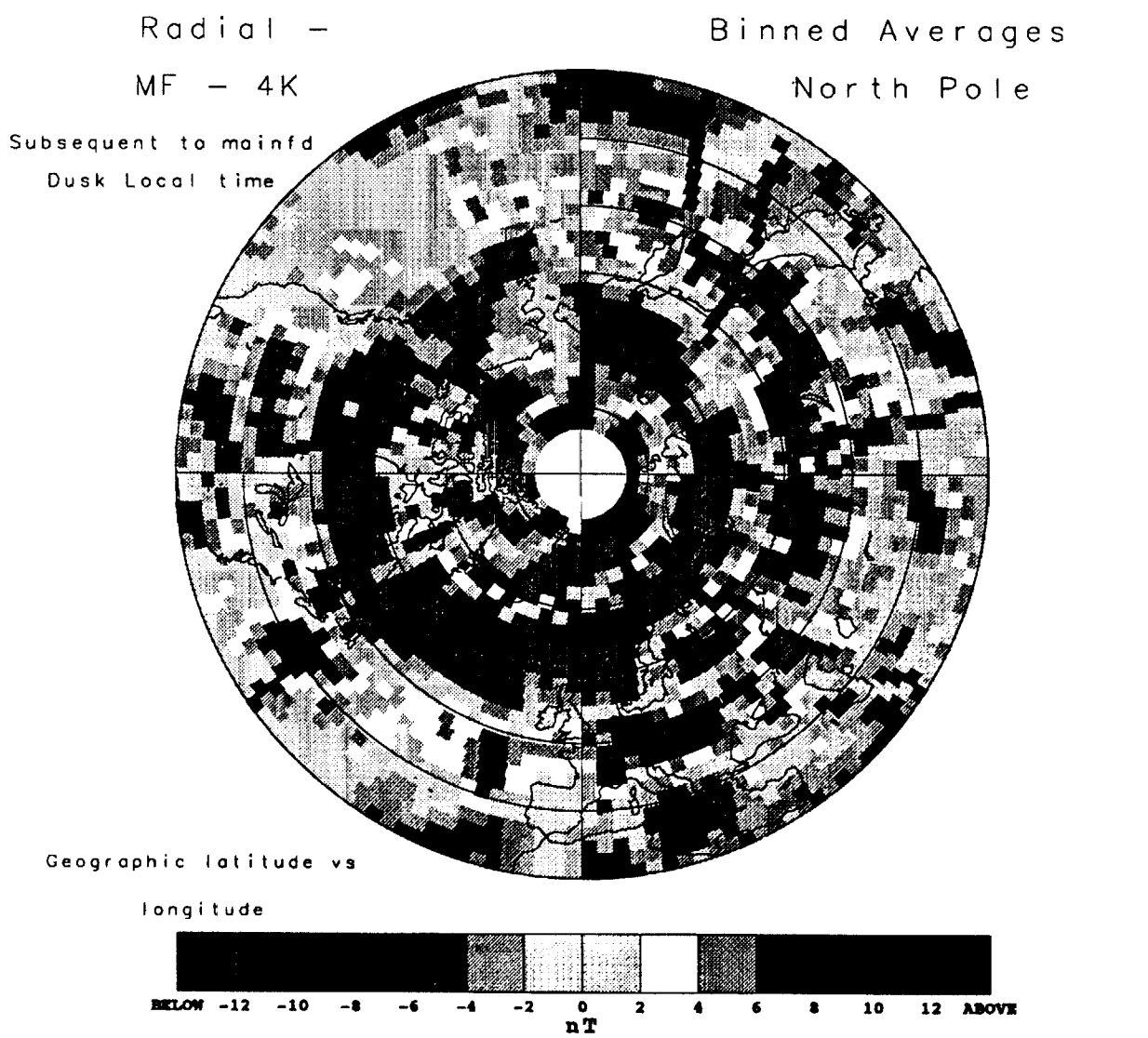
Radial –
MF – 4K
Subsequent to mainfd
Dusk Local time
Binned Averages
North Pole
Geographic latitude vs
longitude
BELOW -12 -10 -8 -6 -4 -2 0 2 4 6 8 10 12 ABOVE
nT
npolebin.f 11-14-92

FIG. 6b

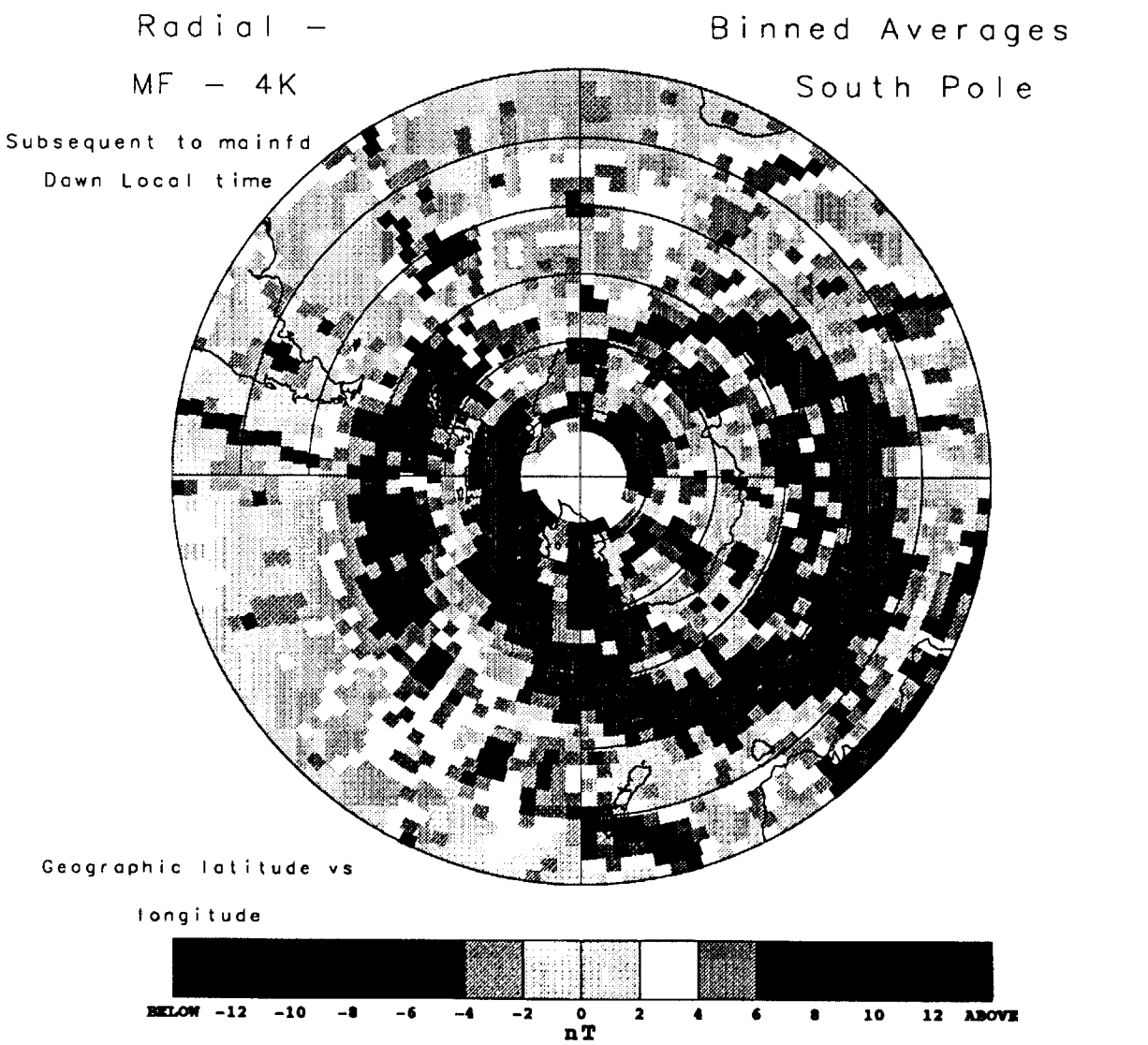
Radial –
MF – 4K
Subsequent to mainfd
Dawn Local time
Binned Averages
South Pole
Geographic latitude vs
longitude
BELOW -12 -10 -8 -6 -4 -2 0 2 4 6 8 10 12 ABOVE
nT
spolebin.f 11-19-92

FIG. 6c

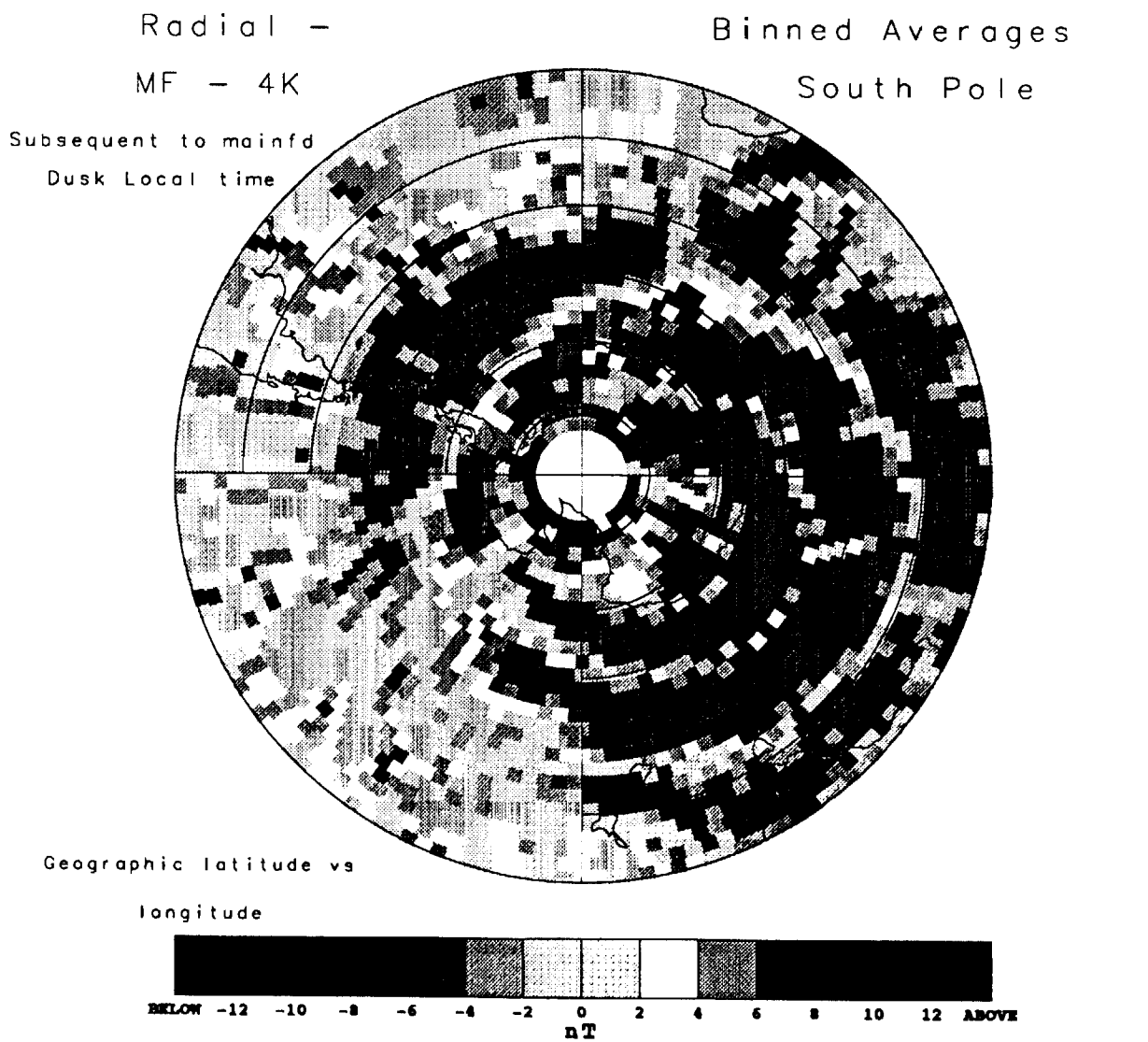
Radial –
MF – 4K
Subsequent to mainfd
Dusk Local time
Binned Averages
South Pole
Geographic latitude vs
longitude
BELOW -12 -10 -8 -6 -4 -2 0 2 4 6 8 10 12 ABOVE
nT
spolebin.f 11-19-92

FIG. 6d

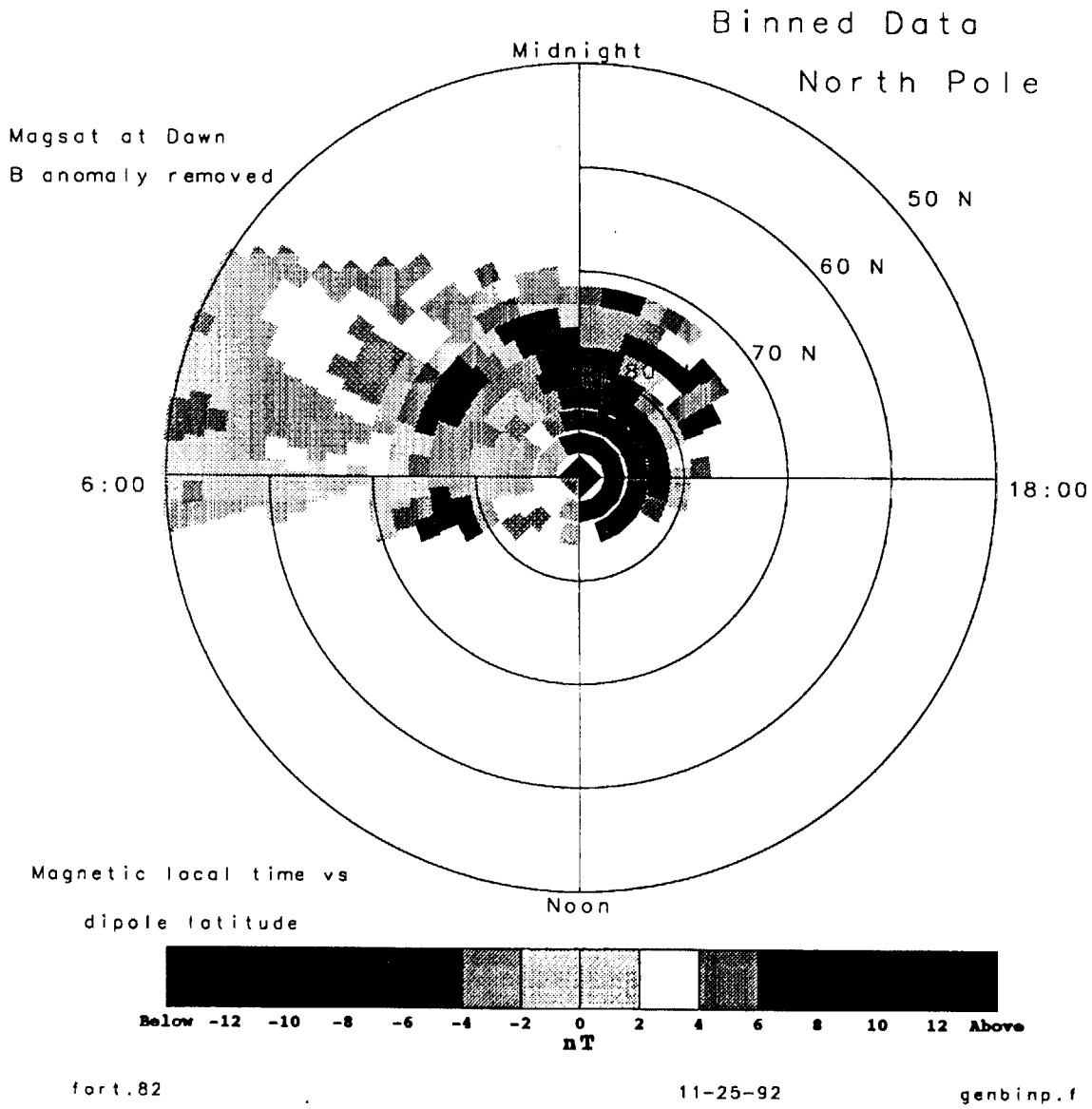
Binned Data
North Pole
Midnight
Magsat at Dawn
B anomaly removed
50 N
60 N
70 N
6:00
18:00
Noon
Magnetic local time vs
dipole latitude
Below -12 -10 -8 -6 -4 -2 0 2 4 6 8 10 12 Above
nT
fort.82
11-25-92
genbinp.f

FIG. 7a

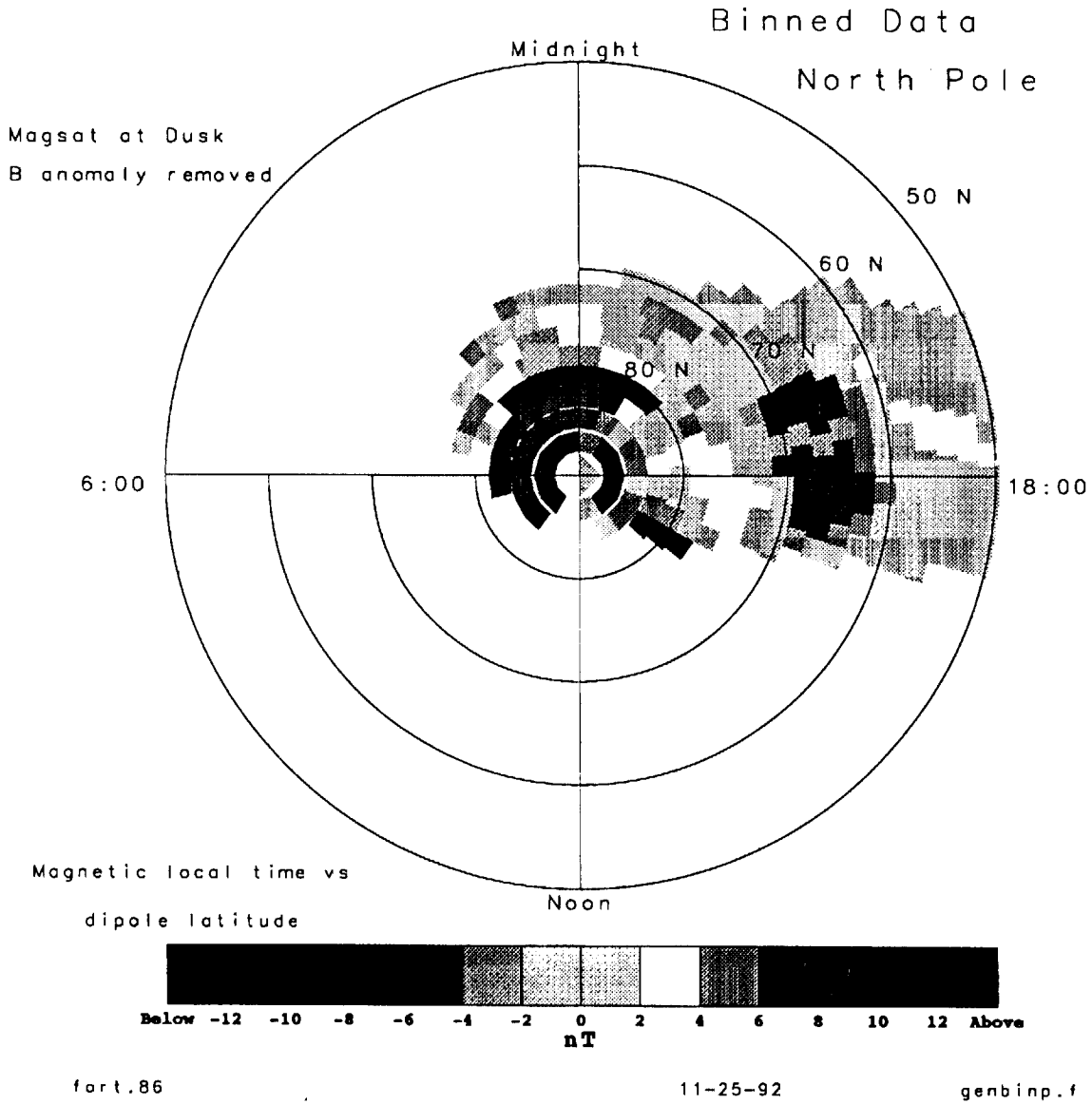
Binned Data
North Pole
Midnight
Magsat at Dusk
B anomaly removed
50 N
60 N
70 N
80 N
6:00
18:00
Noon
Magnetic local time vs
dipole latitude
Below -12 -10 -8 -6 -4 -2 0 2 4 6 8 10 12 Above
nT
fort.86
11-25-92
genbinp.f

FIG. 7b

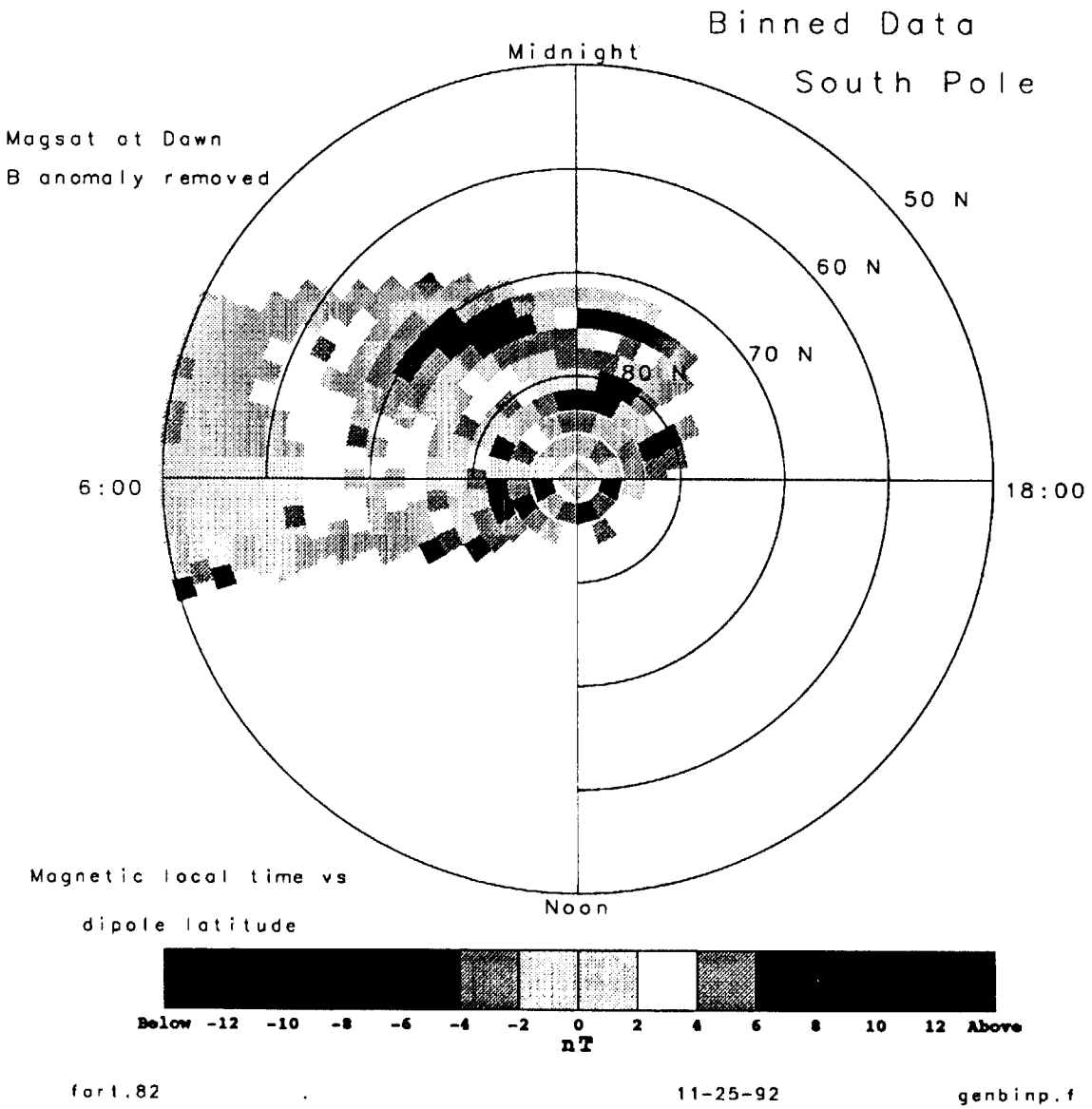
Binned Data
South Pole
Midnight
Magsat at Dawn
B anomaly removed
50 N
60 N
70 N
80 N
6:00
18:00
Noon
Magnetic local time vs
dipole latitude
Below -12 -10 -8 -6 -4 -2 0 2 4 6 8 10 12 Above
nT
fort.82
11-25-92
genbinp.f

FIG. 7c

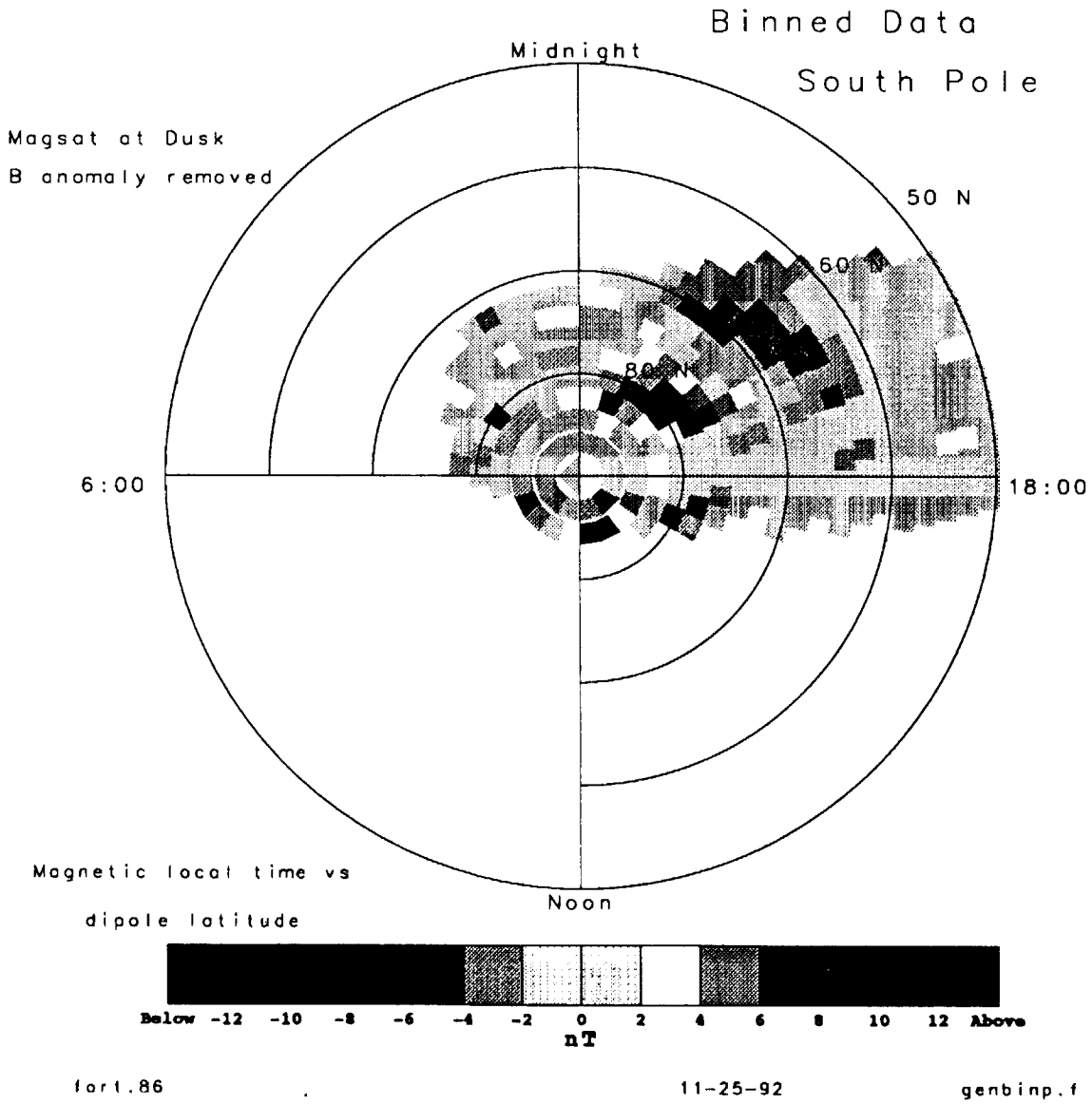
Binned Data
South Pole
Midnight
Magsat at Dusk
B anomaly removed
50 N
60 N
80 N
6:00
18:00
Noon
Magnetic local time vs
dipole latitude
Below -12 -10 -8 -6 -4 -2 0 2 4 6 8 10 12 Above
nT
fort.86
11-25-92
genbinp.f

FIG. 7d

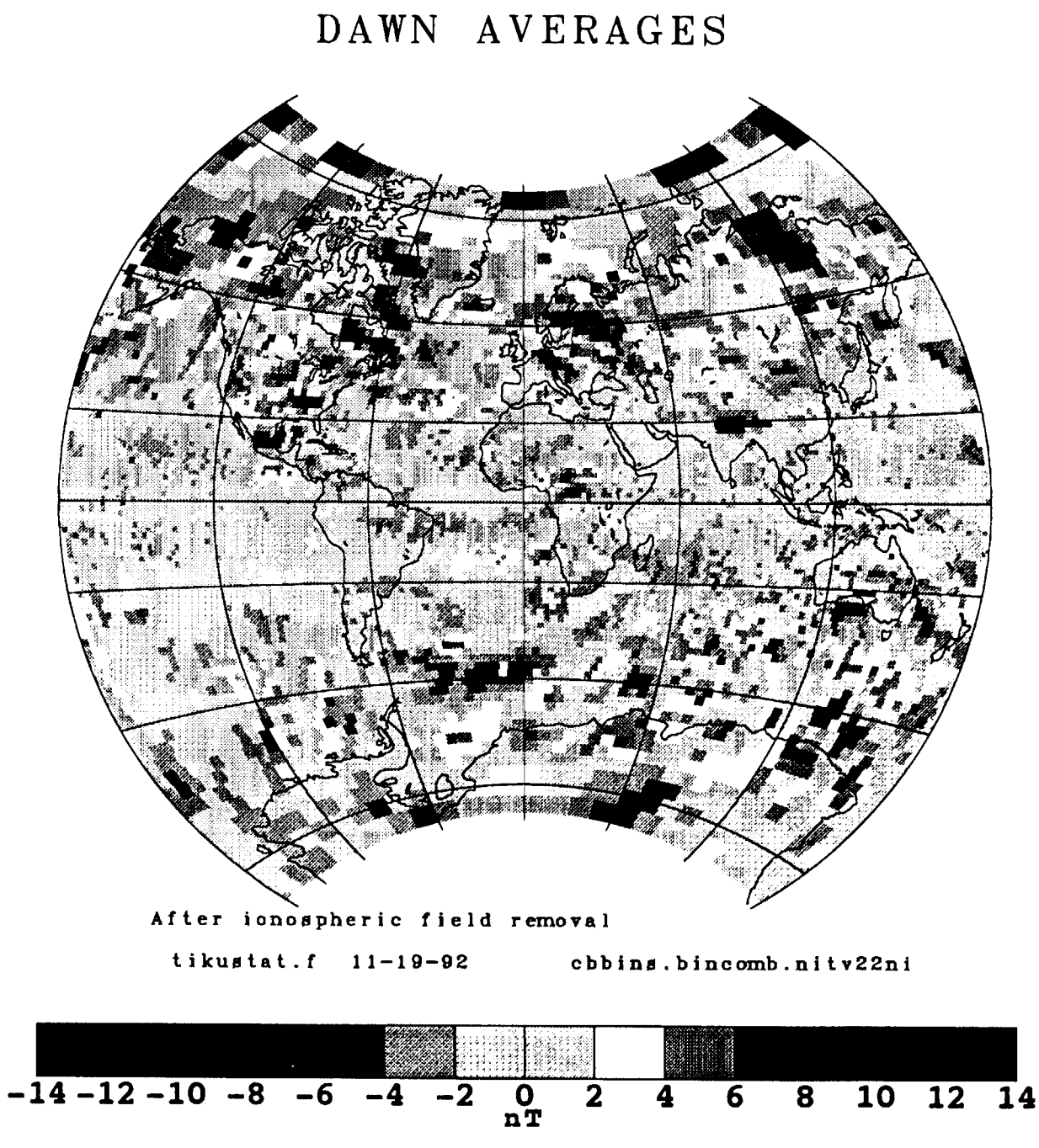
DAWN AVERAGES
After ionospheric field removal
tikustat.f 11-19-92
cbbins.bincomb.nitv22ni
-14 -12 -10 -8 -6 -4 -2 0 2 4 6 8 10 12 14
nT

FIG. 8

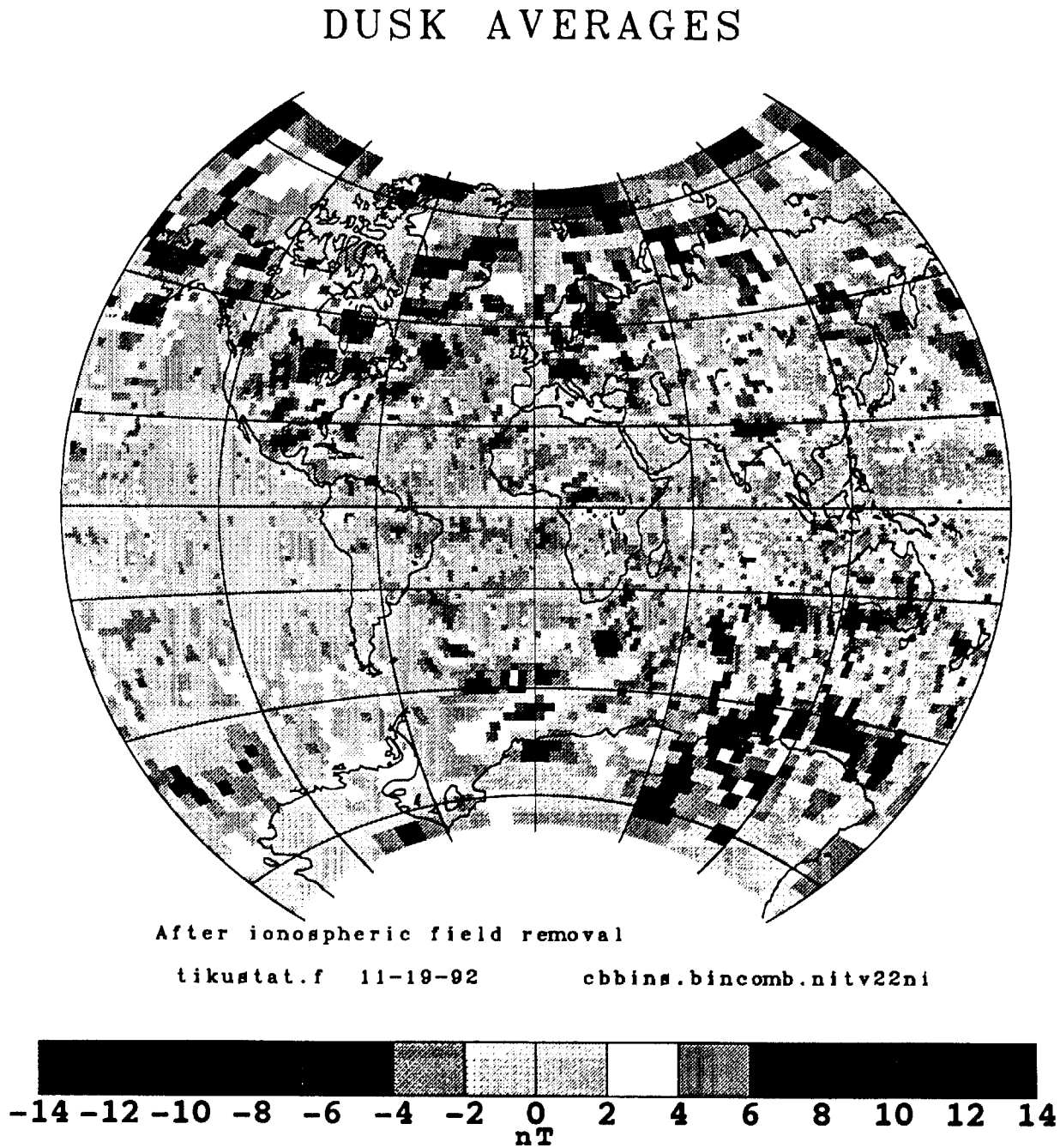
DUSK AVERAGES
After ionospheric field removal
tikustat.f 11-19-92
cbbins.bincomb.nitv22ni
-14 -12 -10 -8 -6 -4 -2 0 2 4 6 8 10 12 14
nT

FIG. 9

DAWN - DUSK

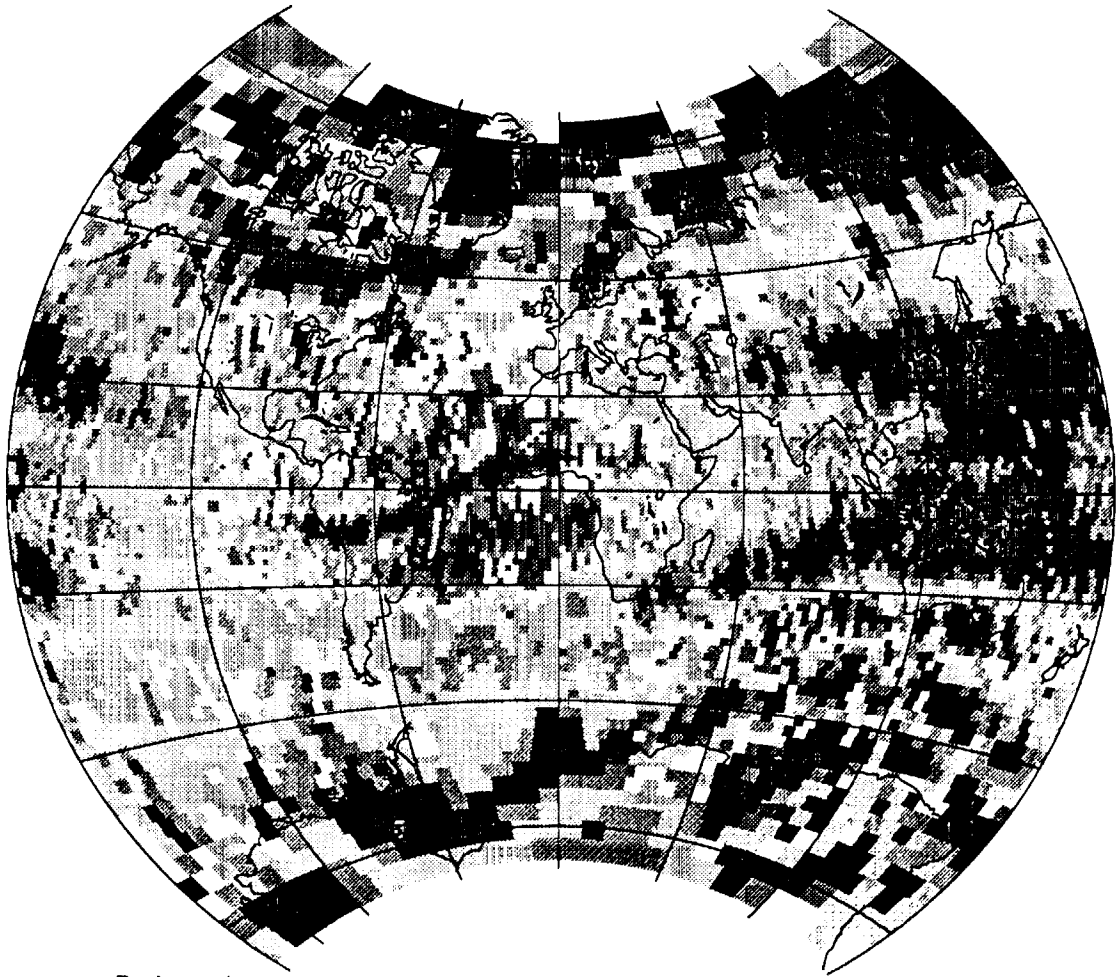

Prior to ionospheric field removal

tikustat.f 11-19-92 cbbins.bincomb

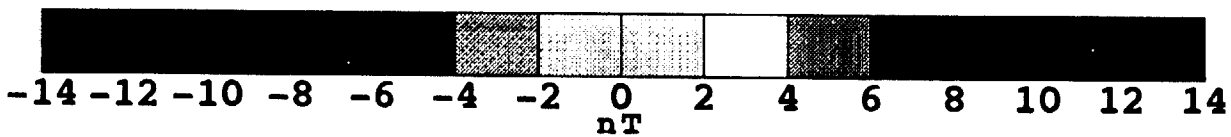

FIG. 10a

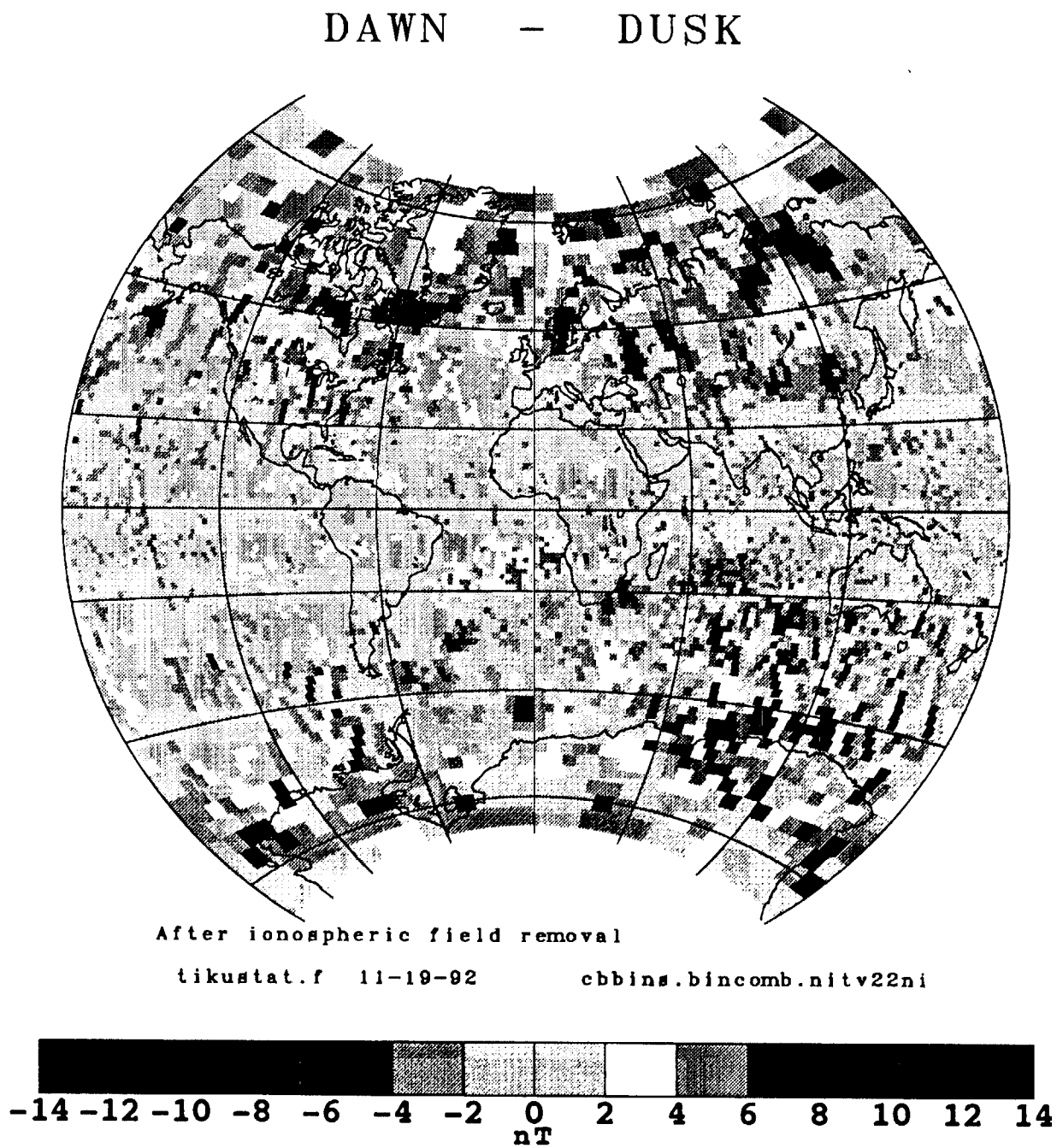
DAWN - DUSK
After ionospheric field removal
tikustat.f 11-19-92
cbbins.bincomb.nitv22ni
-14 -12 -10 -8 -6 -4 -2 0 2 4 6 8 10 12 14
nT

FIG. 10b

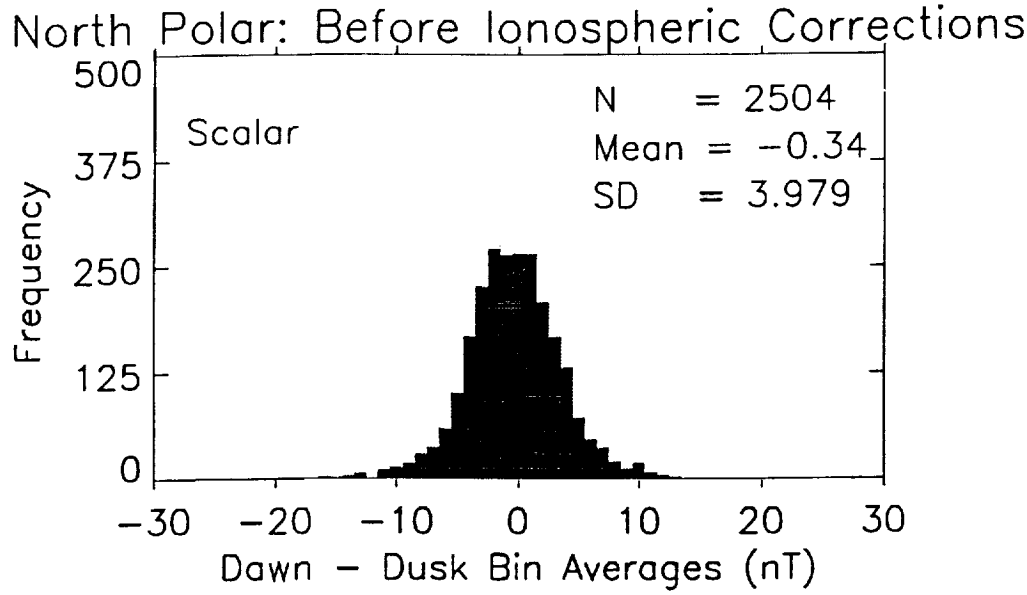
North Polar: Before Ionospheric Corrections
Scalar
N = 2504
Mean = −0.34
SD = 3.979
Frequency
500
375
250
125
0
−30
−20
−10
0
10
20
30
Dawn − Dusk Bin Averages (nT)

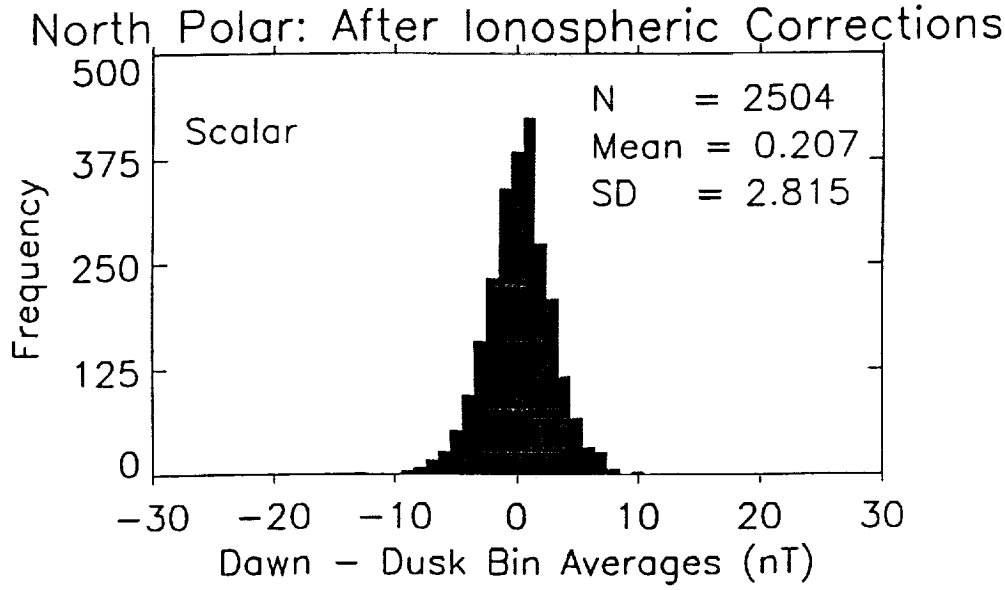
North Polar: After Ionospheric Corrections
Scalar
N = 2504
Mean = 0.207
SD = 2.815
Frequency
500
375
250
125
0
−30
−20
−10
0
10
20
30
Dawn − Dusk Bin Averages (nT)

FIG. 11a

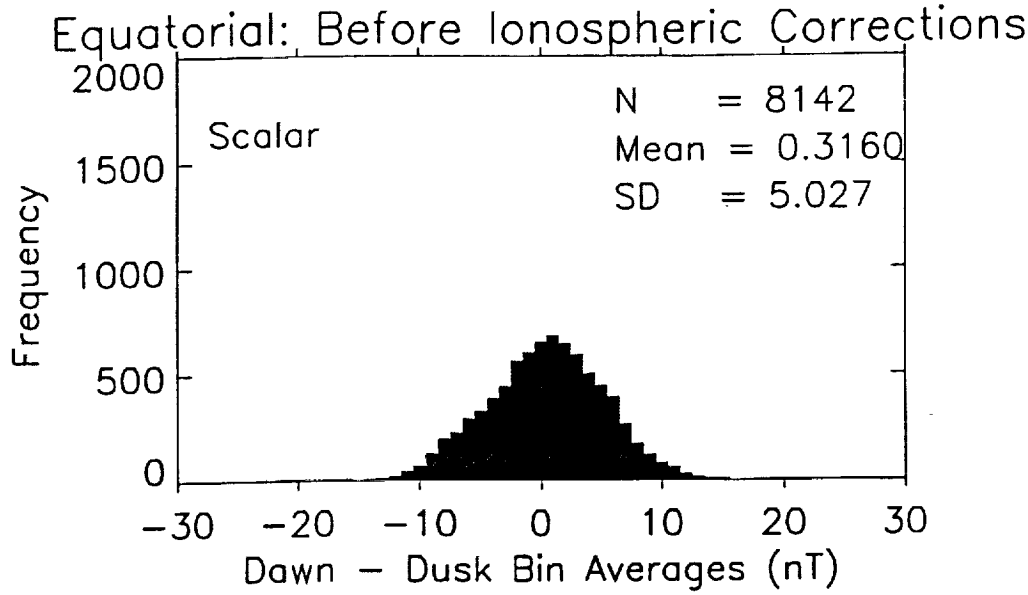
Equatorial: Before Ionospheric Corrections
Scalar
N = 8142
Mean = 0.3160
SD = 5.027
Frequency
2000
1500
1000
500
0
−30 −20 −10 0 10 20 30
Dawn − Dusk Bin Averages (nT)

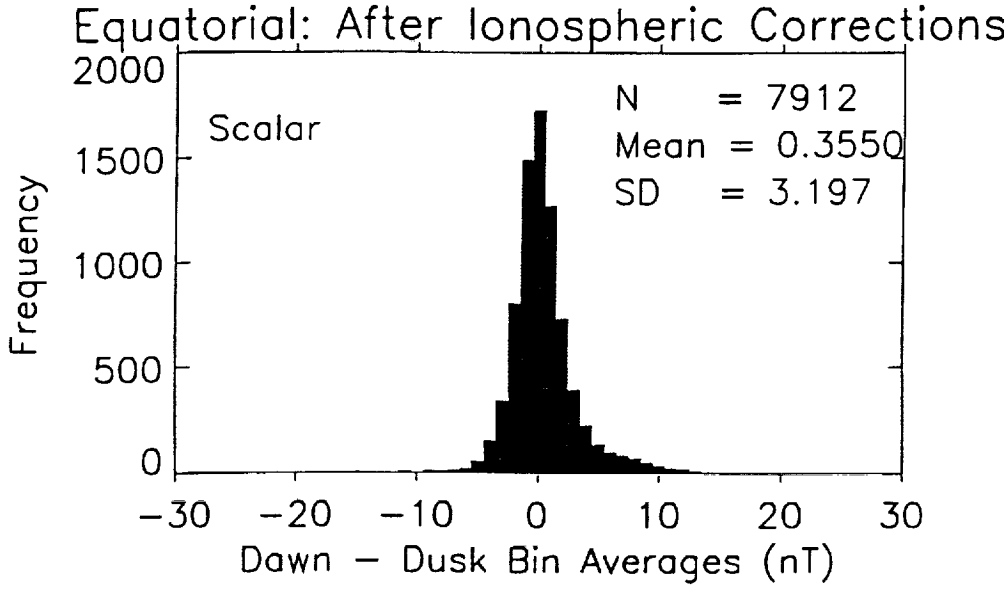
Equatorial: After Ionospheric Corrections
Scalar
N = 7912
Mean = 0.3550
SD = 3.197
Frequency
2000
1500
1000
500
0
−30 −20 −10 0 10 20 30
Dawn − Dusk Bin Averages (nT)

FIG. 11b

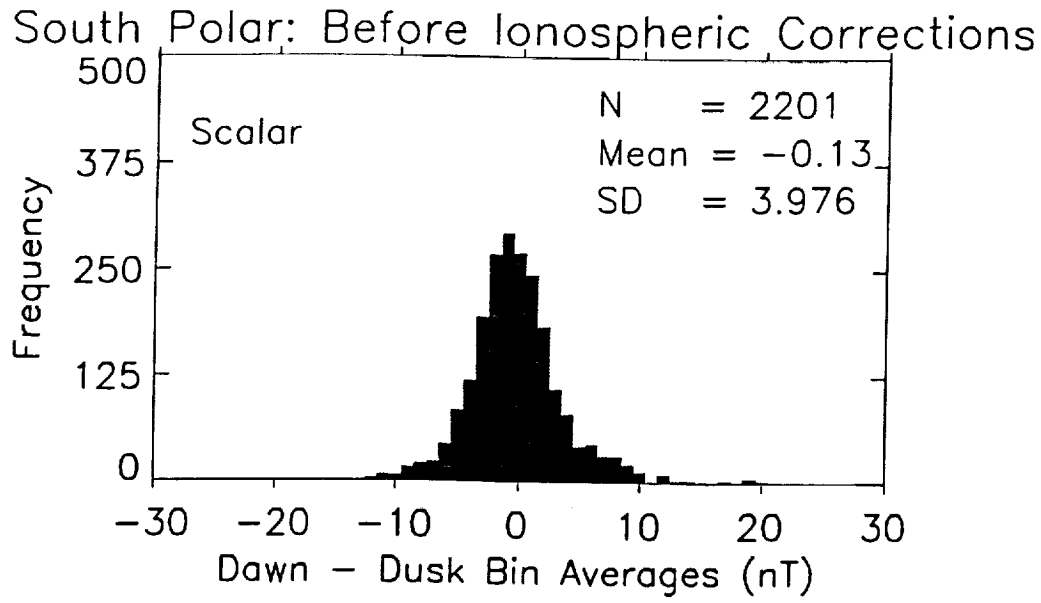
South Polar: Before Ionospheric Corrections
Scalar
N = 2201
Mean = −0.13
SD = 3.976
Frequency
500
375
250
125
0
−30
−20
−10
0
10
20
30
Dawn − Dusk Bin Averages (nT)

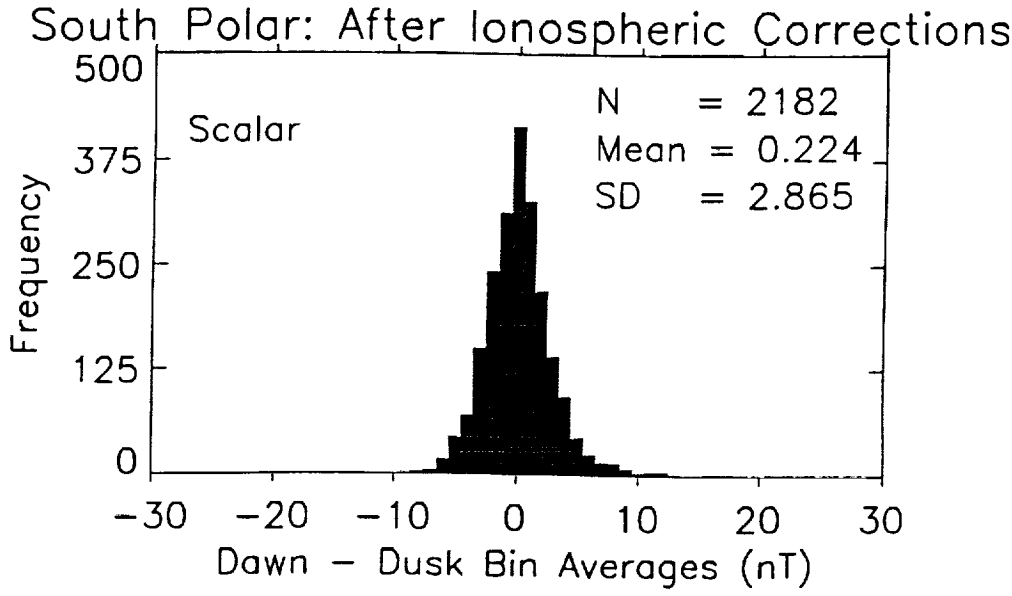
South Polar: After Ionospheric Corrections
Scalar
N = 2182
Mean = 0.224
SD = 2.865
Frequency
500
375
250
125
0
−30
−20
−10
0
10
20
30
Dawn − Dusk Bin Averages (nT)

FIG. 11c

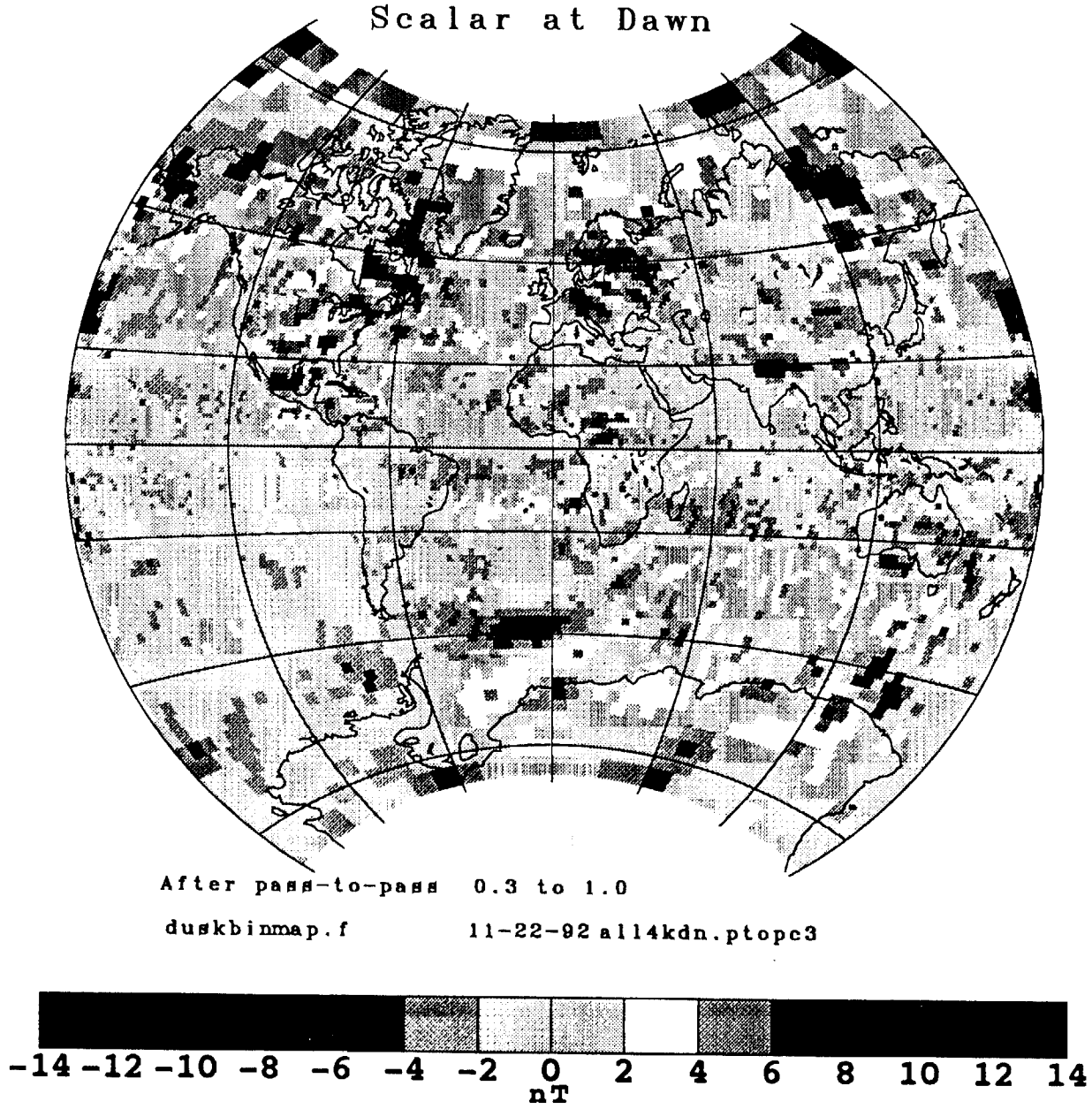
Scalar at Dawn
After pass-to-pass 0.3 to 1.0
duskbinmap.f 11-22-92 all4kdn.ptopc3
-14 -12 -10 -8 -6 -4 -2 0 2 4 6 8 10 12 14
nT

FIG. 12

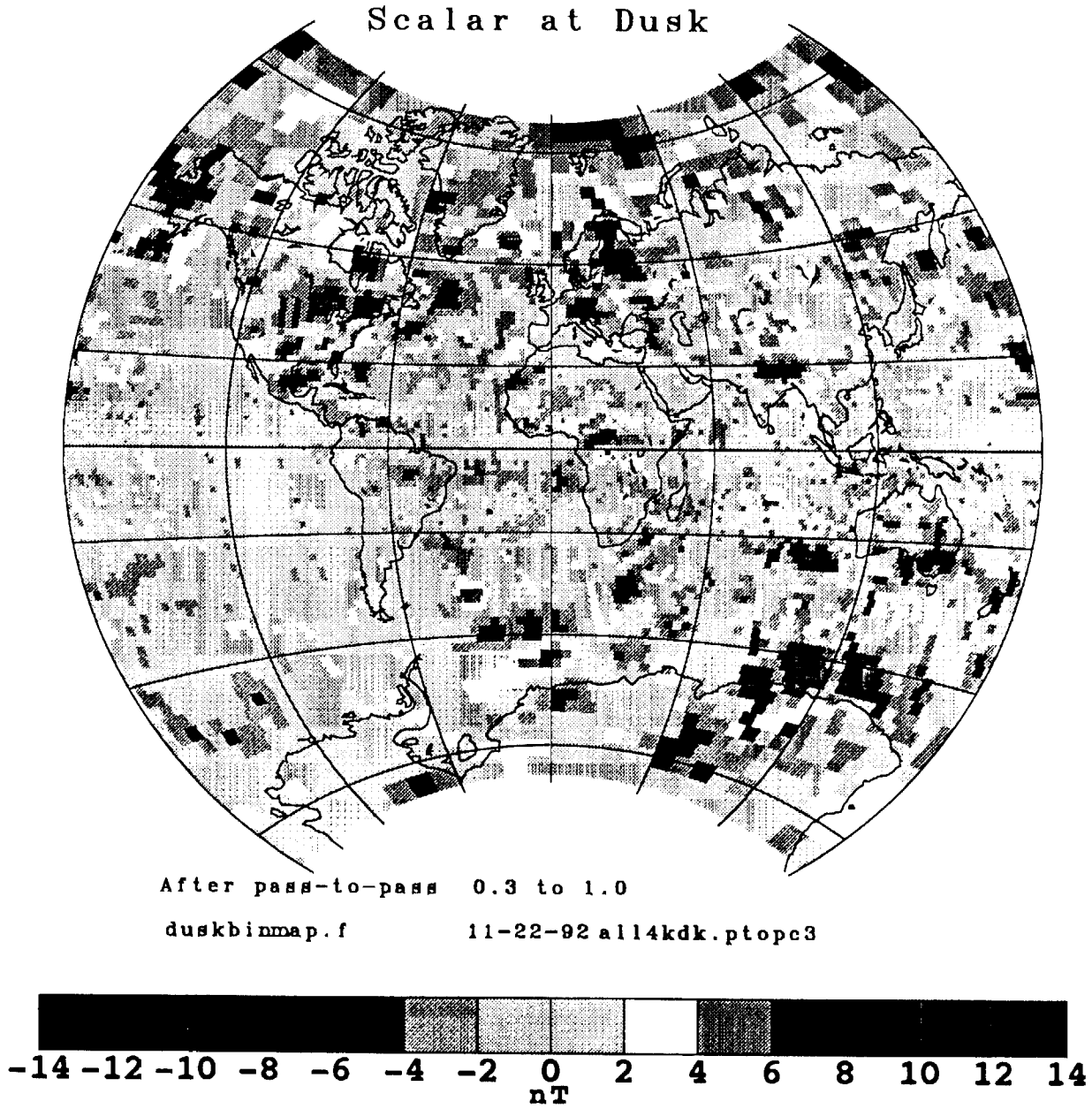
Scalar at Dusk
After pass-to-pass 0.3 to 1.0
duskbinmap.f 11-22-92 all4kdk.ptopc3
-14 -12 -10 -8 -6 -4 -2 0 2 4 6 8 10 12 14
nT

FIG. 13

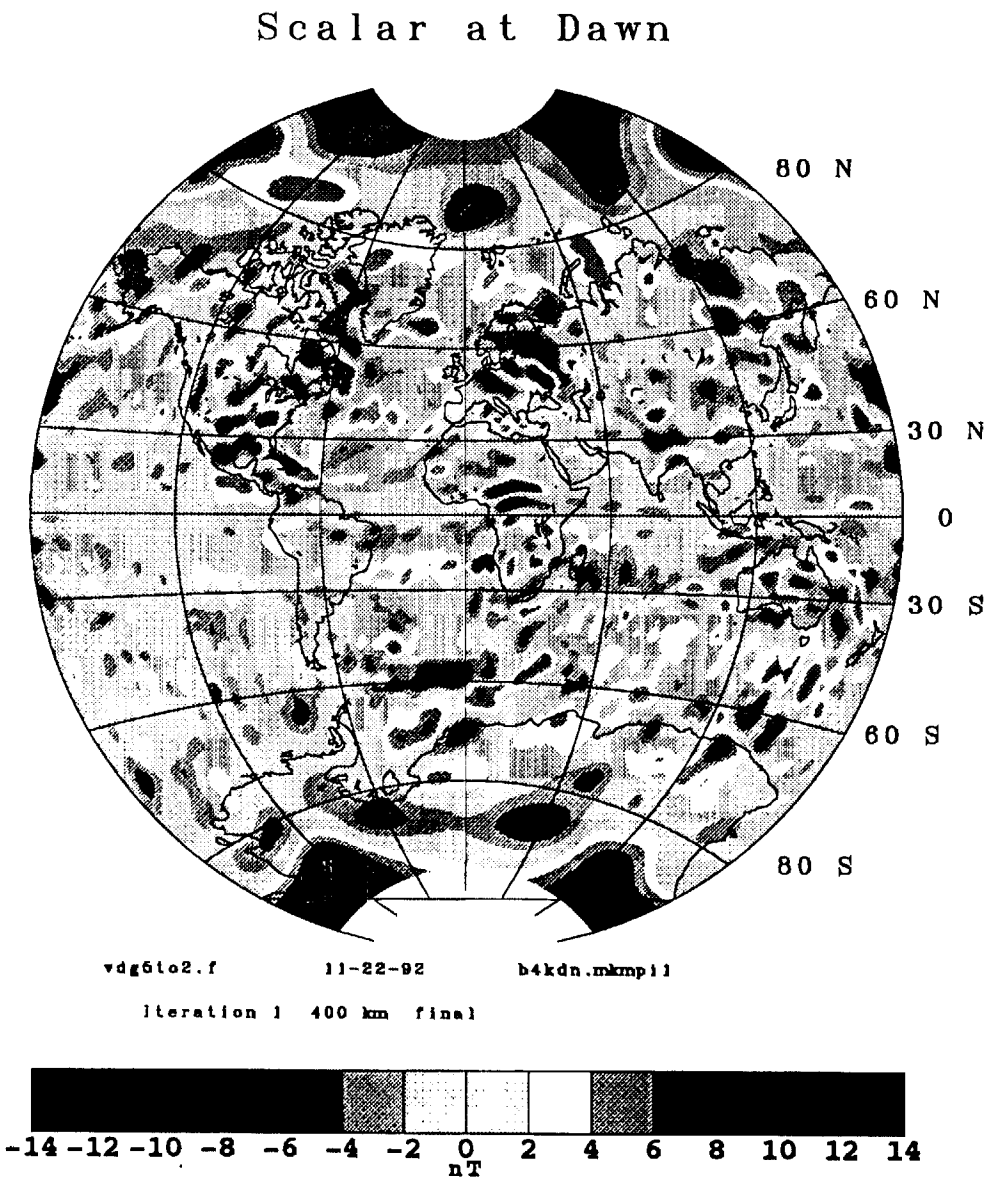
Scalar at Dawn
80 N
60 N
30 N
0
30 S
60 S
80 S
vdg6to2.f
11-22-92
b4kdn.mkmpll
Iteration 1 400 km final
-14 -12 -10 -8 -6 -4 -2 0 2 4 6 8 10 12 14
nT

FIG. 14

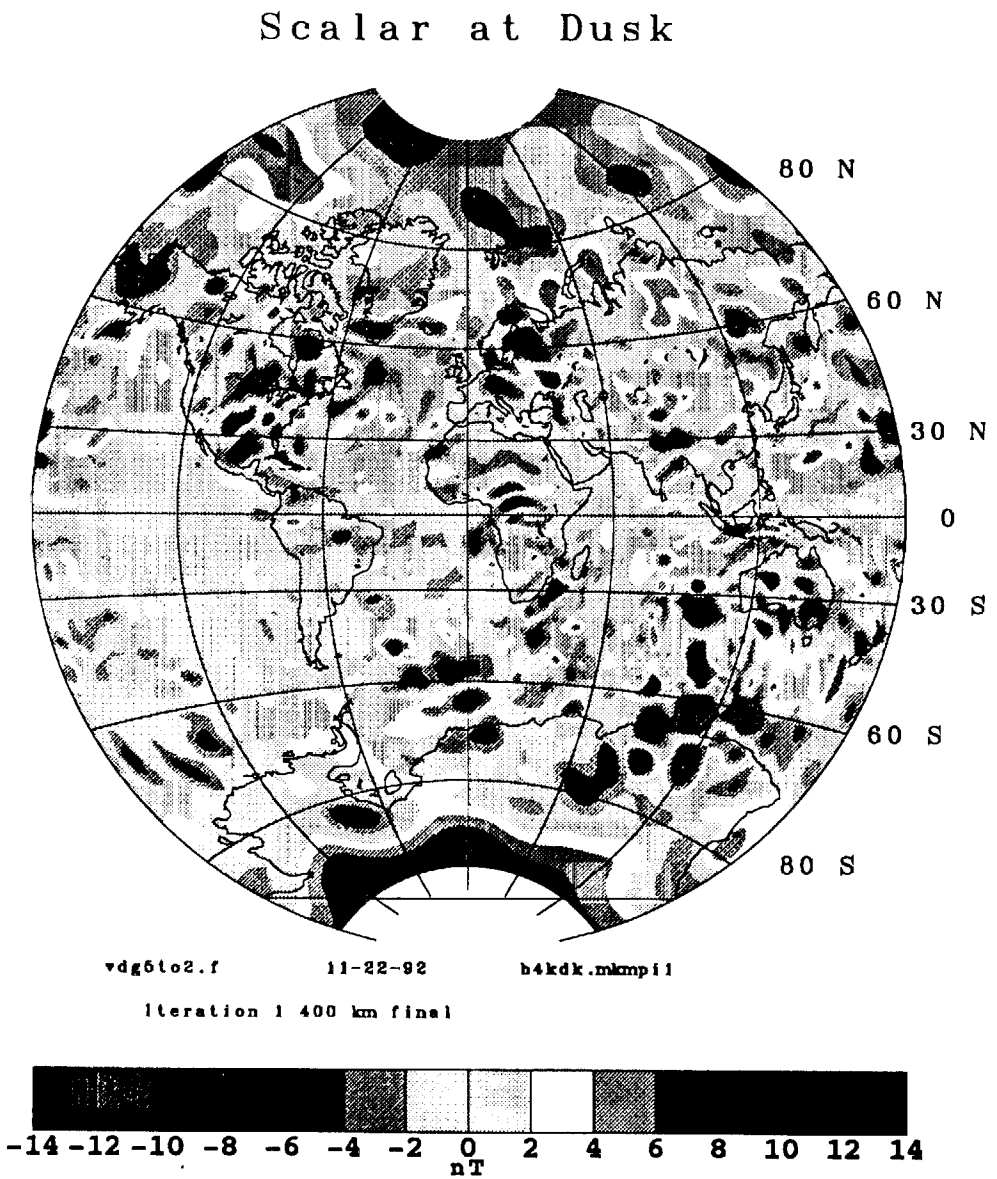
Scalar at Dusk
80 N
60 N
30 N
0
30 S
60 S
80 S
vdg6to2.f
11-22-92
b4kdk.mkmpil
Iteration 1 400 km final
-14 -12 -10 -8 -6 -4 -2 0 2 4 6 8 10 12 14
nT

FIG. 15

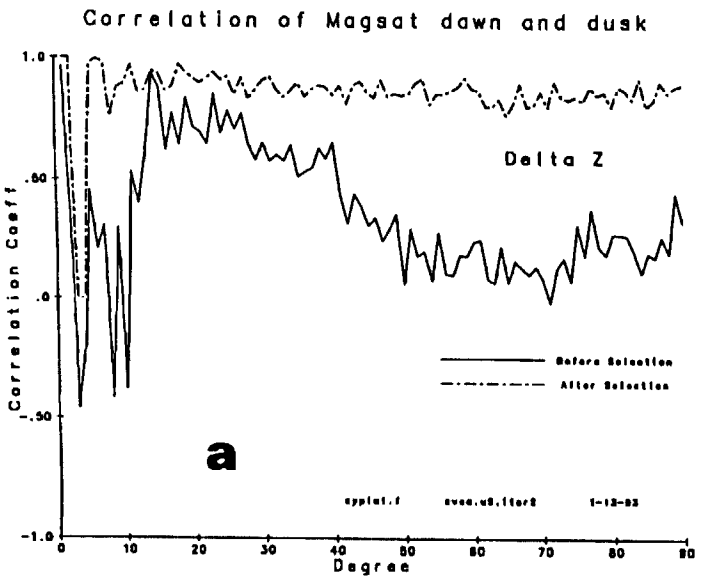
Correlation of Magsat dawn and dusk
Delta Z
Before Selection
After Selection
a
Correlation Coeff
Degree

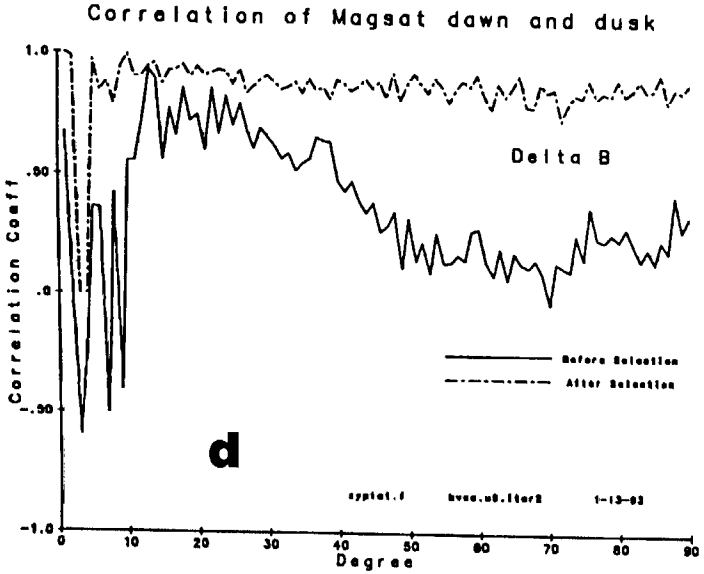
Correlation of Magsat dawn and dusk
Delta B
Before Selection
After Selection
d
Correlation Coeff
Degree

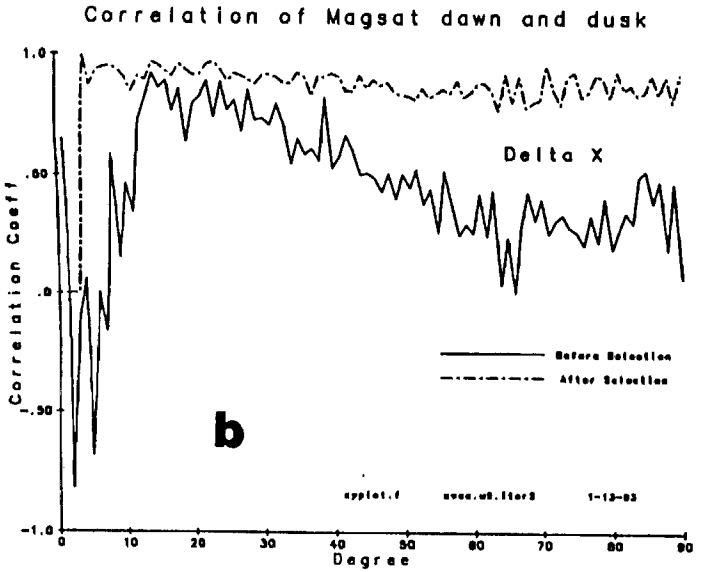
Correlation of Magsat dawn and dusk
Delta X
Before Selection
After Selection
b
Correlation Coeff
Degree

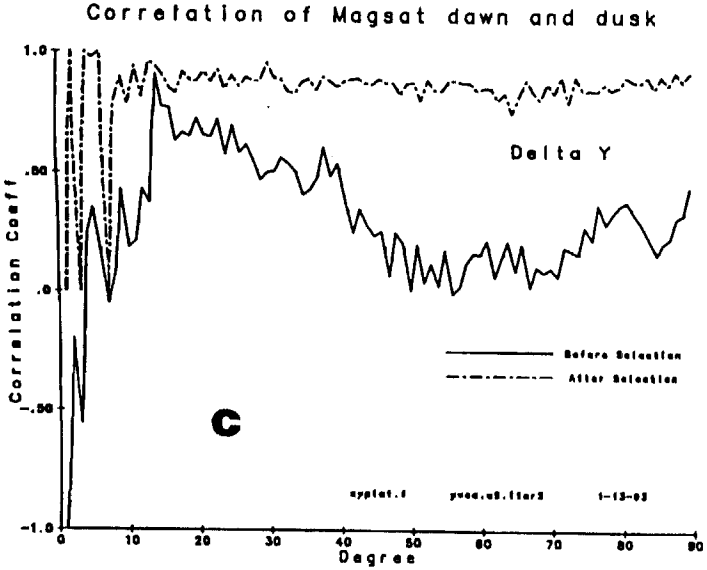
Correlation of Magsat dawn and dusk
Delta Y
Before Selection
After Selection
c
Correlation Coeff
Degree

FIG. 16

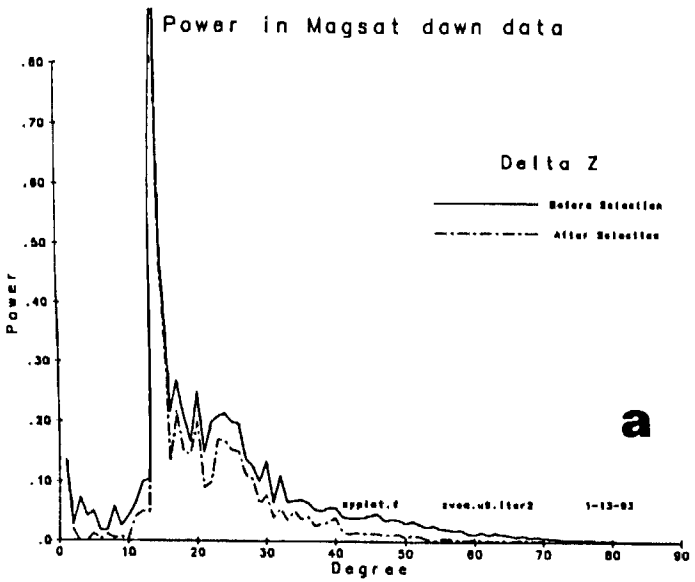
Power in Magsat dawn data
Delta Z
Before Selection
After Selection
Power
Degree
a

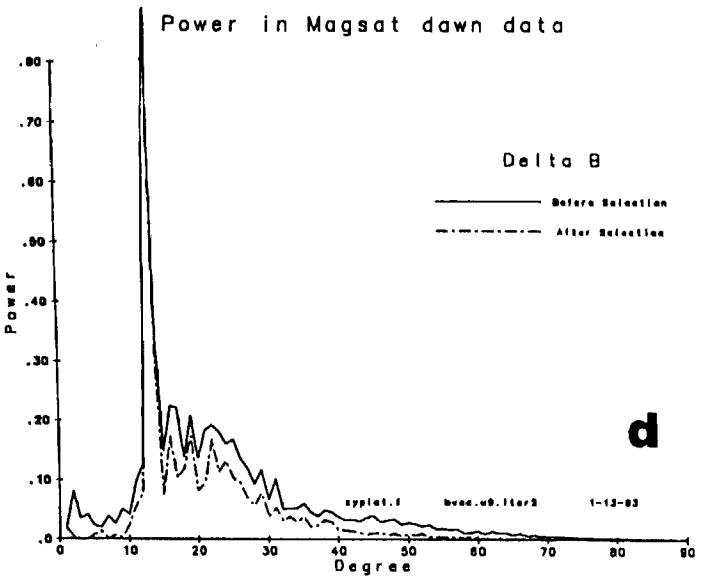
Power in Magsat dawn data
Delta B
Before Selection
After Selection
Power
Degree
d

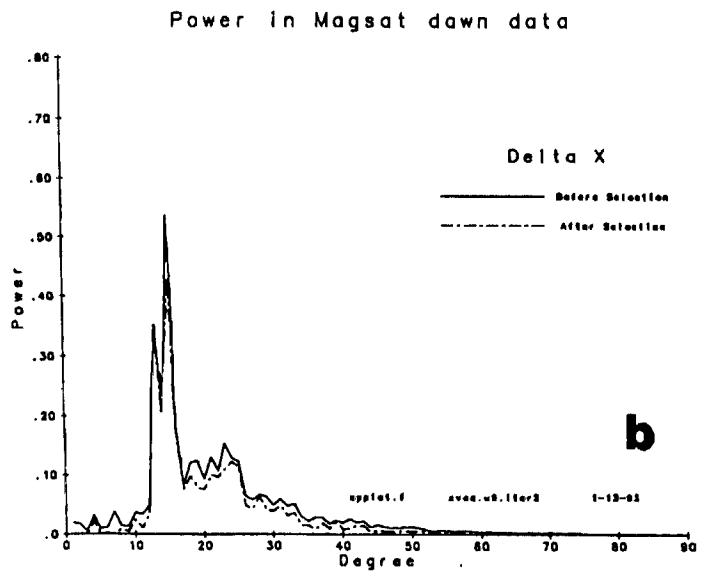
Power in Magsat dawn data
Delta X
Before Selection
After Selection
Power
Degree
b

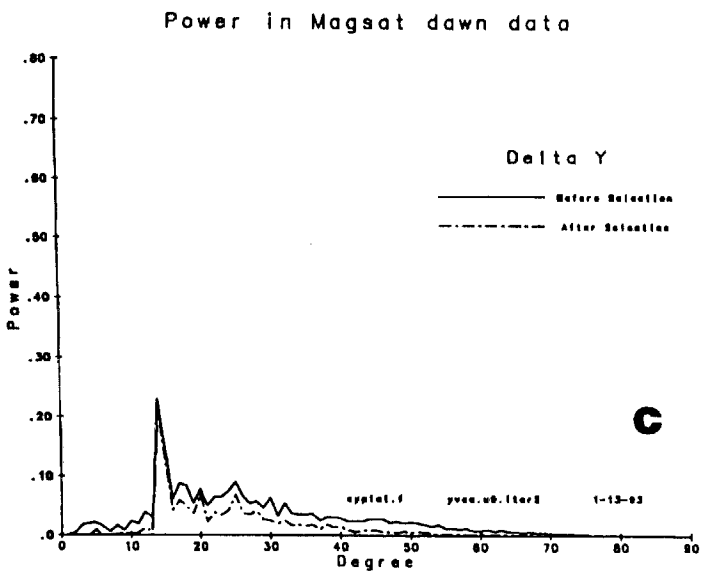
Power in Magsat dawn data
Delta Y
Before Selection
After Selection
Power
Degree
c

FIG. 17

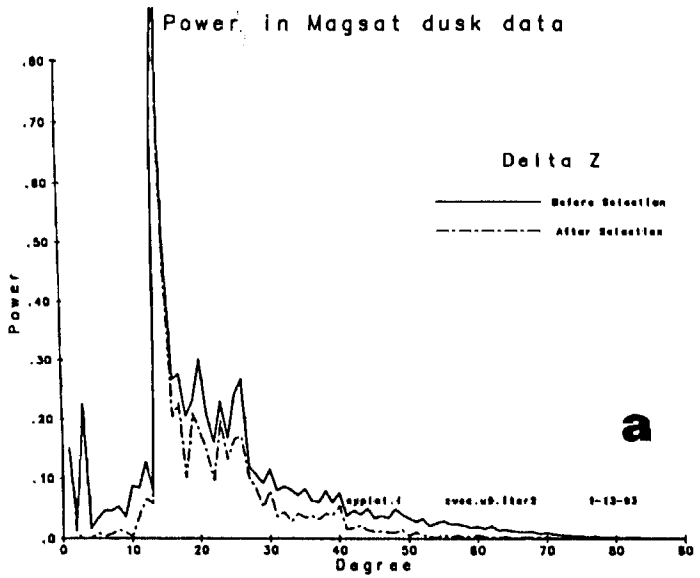
Power in Magsat dusk data
Delta Z
Before Selection
After Selection
Power
Degree
a

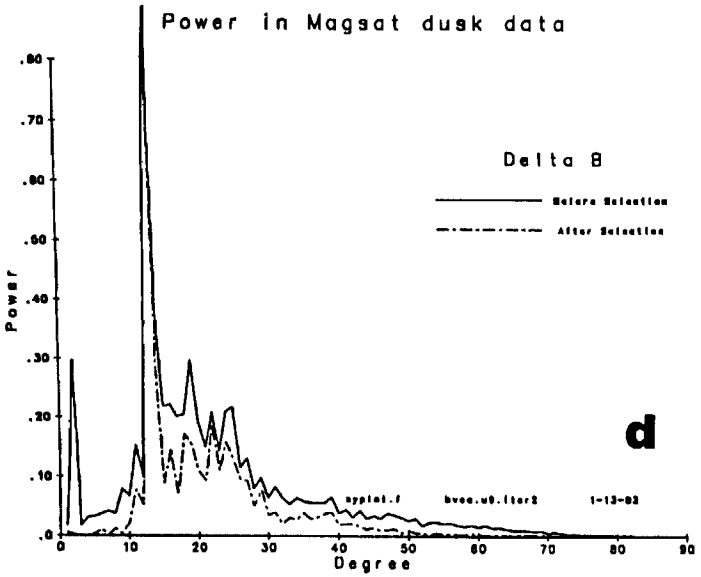
Power in Magsat dusk data
Delta B
Before Selection
After Selection
Power
Degree
d

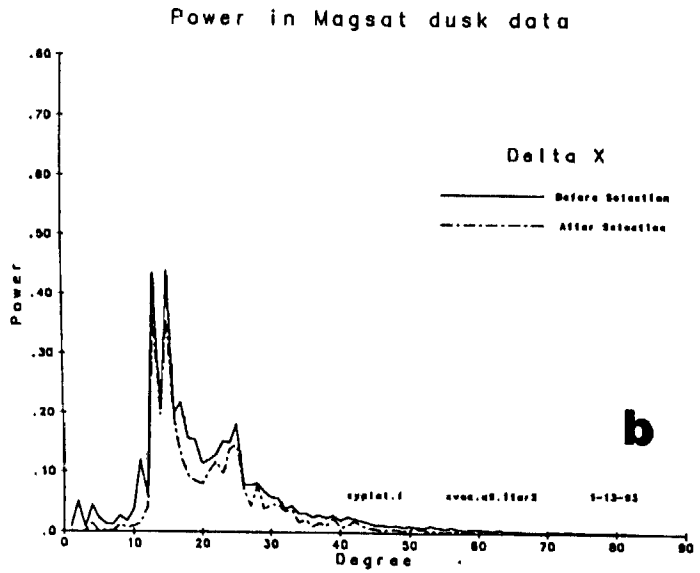
Power in Magsat dusk data
Delta X
Before Selection
After Selection
Power
Degree
b

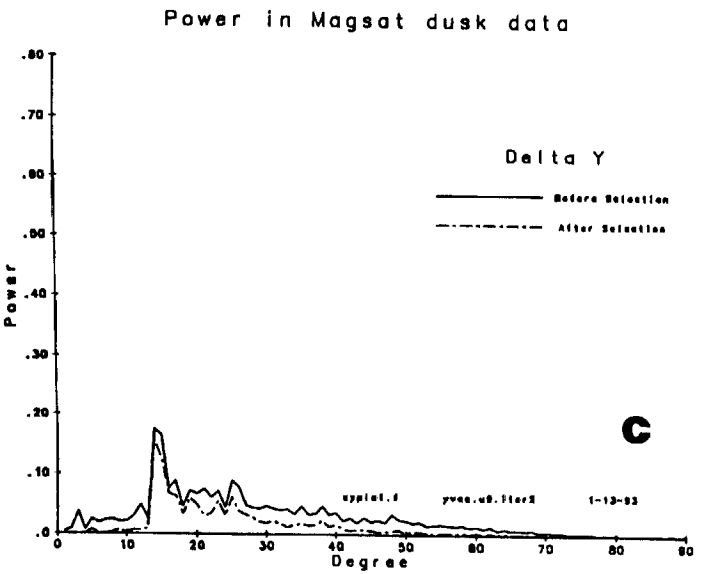
Power in Magsat dusk data
Delta Y
Before Selection
After Selection
Power
Degree
c

FIG. 18

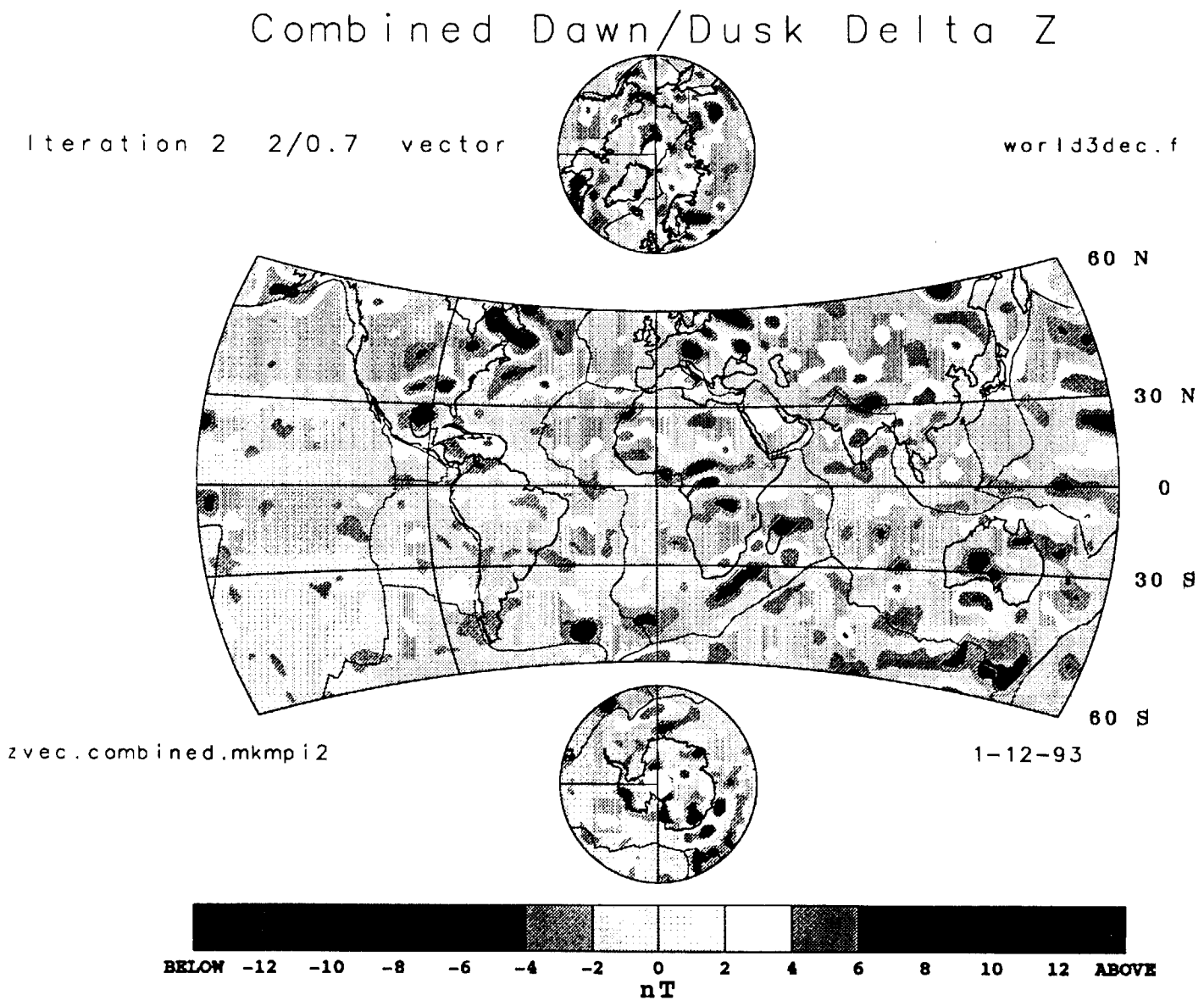
Combined Dawn/Dusk Delta Z
Iteration 2 2/0.7 vector
world3dec.f
60 N
30 N
0
30 S
60 S
zvec.combined.mkmpi2
1-12-93
BELOW -12 -10 -8 -6 -4 -2 0 2 4 6 8 10 12 ABOVE
nT

FIG. 19a

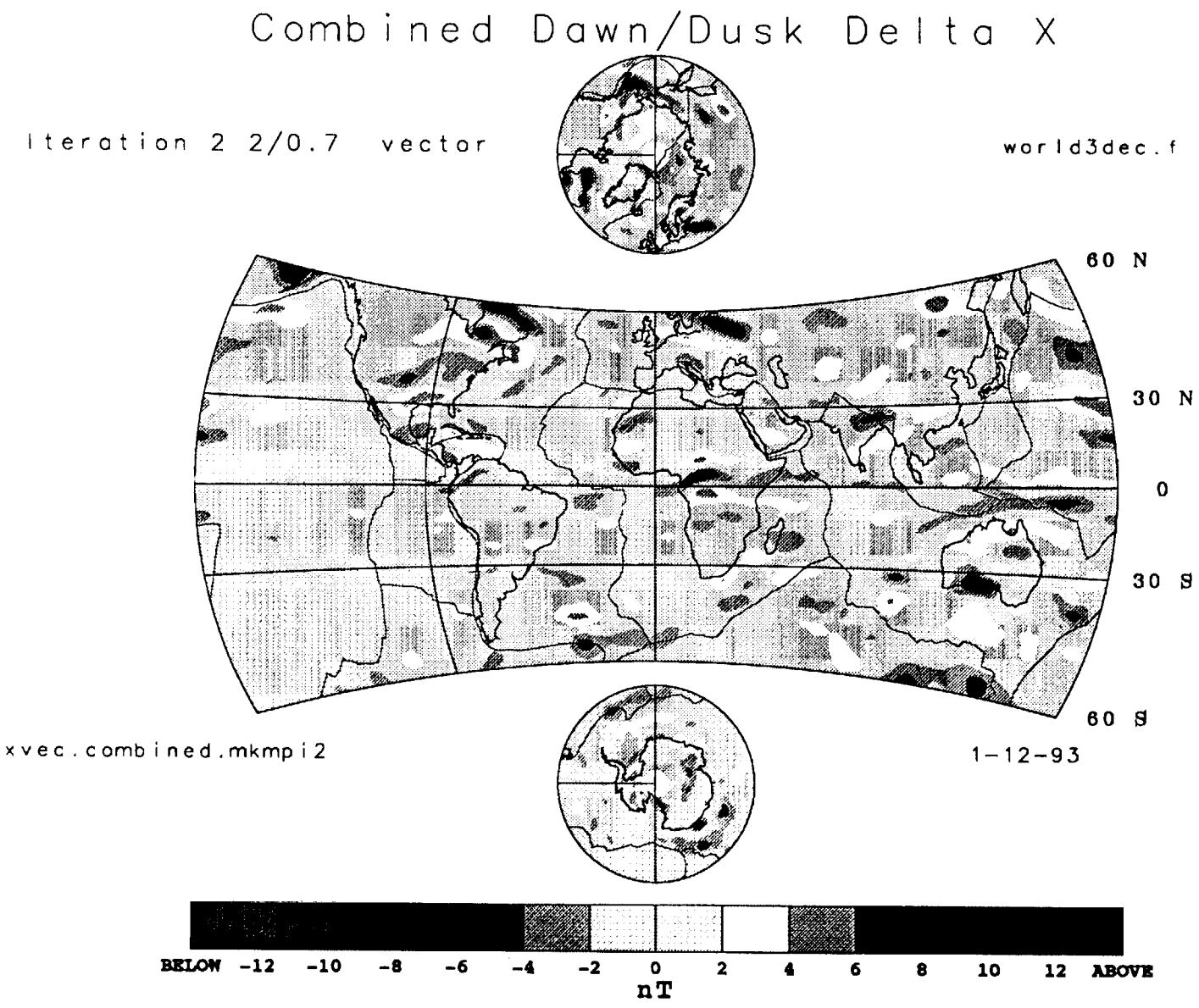
Combined Dawn/Dusk Delta X
Iteration 2 2/0.7 vector
world3dec.f
60 N
30 N
0
30 S
60 S
xvec.combined.mkmpi2
1-12-93
BELOW -12 -10 -8 -6 -4 -2 0 2 4 6 8 10 12 ABOVE
nT

FIG. 19b

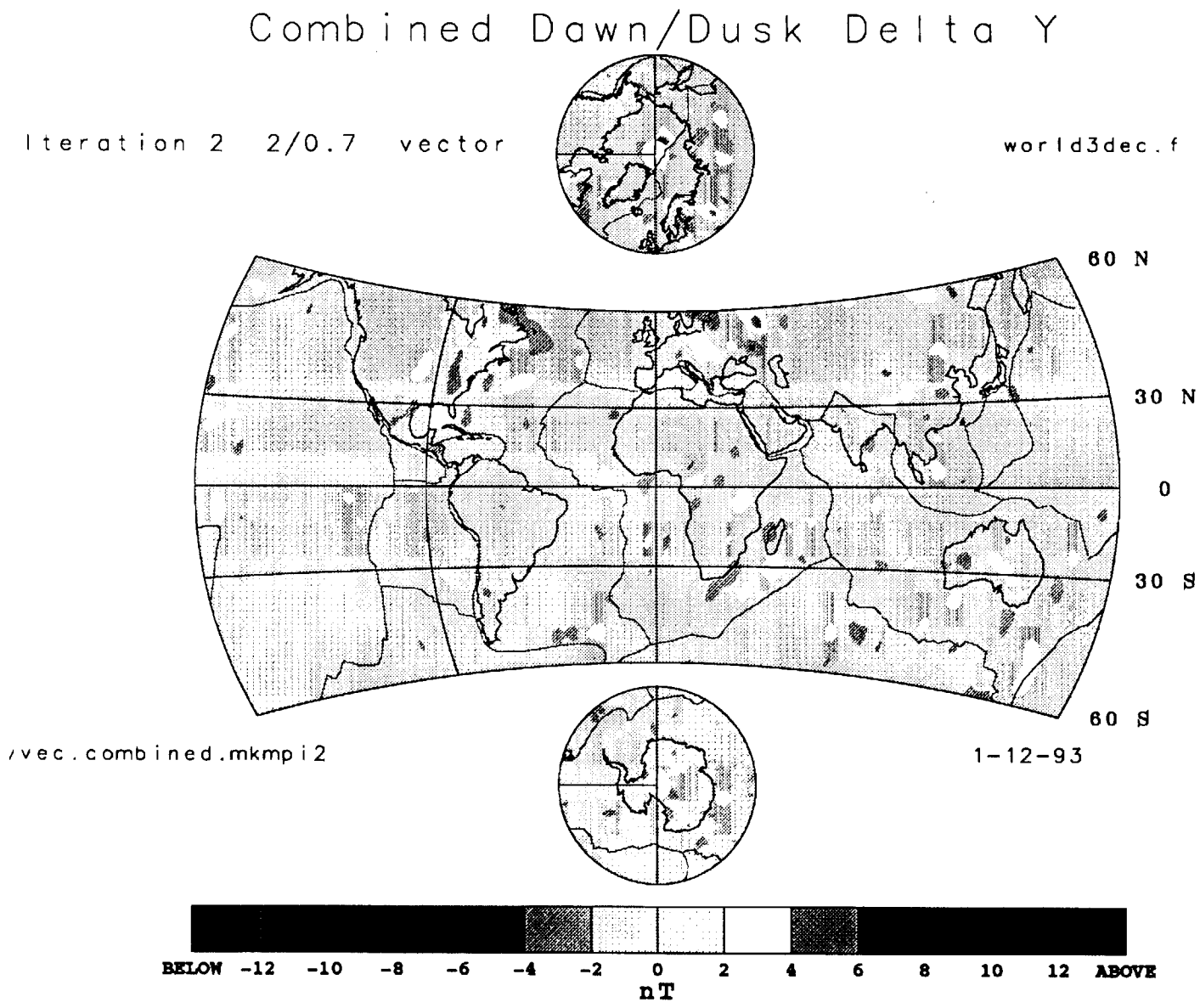
Combined Dawn/Dusk Delta Y
Iteration 2 2/0.7 vector
world3dec.f
60 N
30 N
0
30 S
60 S
/vec.combined.mkmpi2
1-12-93
BELOW -12 -10 -8 -6 -4 -2 0 2 4 6 8 10 12 ABOVE
nT

FIG. 19c

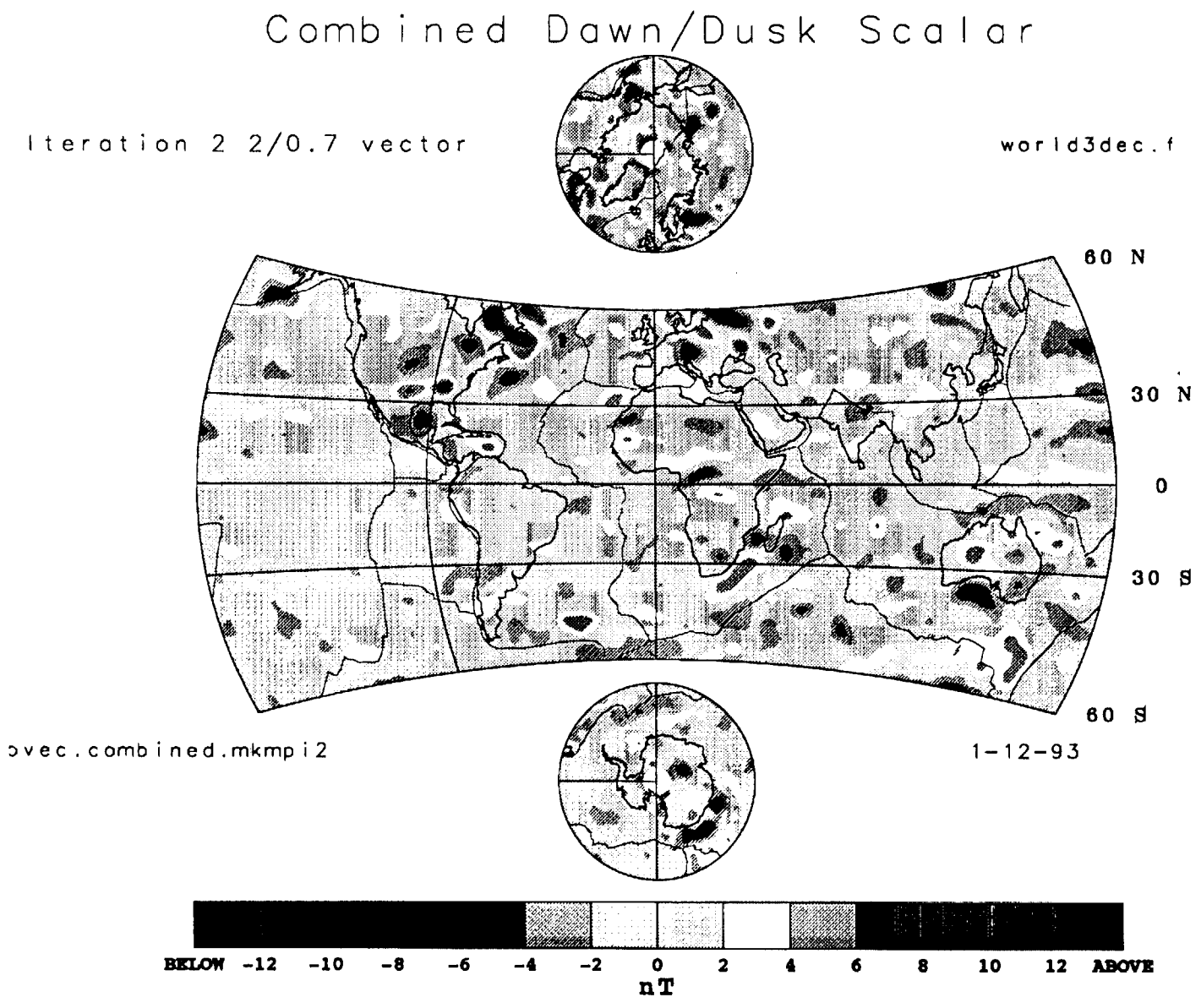
Combined Dawn/Dusk Scalar
Iteration 2 2/0.7 vector
world3dec.f
60 N
30 N
0
30 S
60 S
ovec.combined.mkmpi2
1-12-93
BELOW -12 -10 -8 -6 -4 -2 0 2 4 6 8 10 12 ABOVE
nT

FIG. 19d